Phosphorus and kalium co-doped g-C$_3$N$_4$ with multiple-locus synergies to degrade atrazine: Insights into the depth analysis of the generation and role of singlet oxygen

Yaocheng Deng [a,*], Zhanpeng Zhou [a], Hao Zeng [a], Rongdi Tang [a], Ling Li [a], Jiajia Wang [b], Chengyang Feng [c], Daoxin Gong [a], Lin Tang [b,*], Ying Huang [a,*]

[a] College of Resources & Environment, Hunan Agricultural University, Changsha 410128, PR China
[b] College of Environmental Science and Engineering, Hunan University, Changsha 410082, PR China
[c] KAUST Catalysis Center, Physical Sciences and Engineering Division, King Abdullah University of Science and Technology, Thuwal 23955-6900, Saudi Arabia

ARTICLE INFO

ABSTRACT

In this work, with the help of KH$_2$PO$_4$, a phosphorus and kalium co-doped g-C$_3$N$_4$ with cyano and nitrogen vacancies (PKCN) have been prepared via a simple thermal treatment. The prepared PKCN exhibited excellent singlet oxygen (^{1}O$_2$) generation ability for the highly efficient degradation of atrazine (ATZ), reaching 95% (pH=5) of decomposition efficiency within 60 min under visible light. Density functional theory (DFT) calculation results visualize the role of cyano groups, nitrogen vacancies, K atoms and P atoms, and the synergistic effect of the above four aspects contributed to the three pathways of hole oxidation, energy transfer and dismutation reaction for efficient ^{1}O$_2$ generation. Moreover, the T.E.S.T and soybean culture experiment demonstrated the toxicity of ATZ have been significantly reduced after the photocatalytic process. This work can give deep insights into the roles and synergy of each active unit for designing and synthesizing efficient g-C$_3$N$_4$.

1. Introduction

With the continuous development of intensive agriculture, the overuse of herbicides, especially atrazine (ATZ), has led to serious problems in the ecosystem. Since the stable structure, atrazine can remain toxic and persist in the environment, which is harmful to human health and unfavorable to the sustainable development of agriculture [1]. Compared with conventional techniques, photocatalysis is preferred to be an ideal atrazine degradation strategy. For one thing, photocatalysis is an environmentally friendly and economical technology that can use light directly without any additional energy input. For another thing, the photocatalytic degradation process does not produce secondary pollution and can effectively mineralize atrazine [2,3]. Photocatalytic reaction mainly depends on the active substances produced in the reaction process, such as photogenerated holes (h$^+$), electrons (e$^-$), and reactive oxygen species (ROS) [4]. The substrate of the pollutant degradation process is very complex in practical application. For the treatment of complex substrates, priority oxidation of target organic pollutants is essential because oxidation of non-target chemicals produces undesirable intermediates and has a greater negative impact on the environment. Singlet oxygen (^{1}O$_2$) is a promising active oxidative species because of its preferential oxidation capacity [5,6]. Singlet oxygen owns electrophilicity and tends to preferentially oxidize the electron-rich part of the target [7]. However, the transfer process is normally forbidden ascribed to the spin-flip restriction between the ground state and singlet state oxygen. Although singlet oxygen can be generated through photosensitizers such as porphyrins, organic dyes, and noble metals, most of them own defects such as poor hydrophilicity, low quantum yield, and high cost, which restrict their applications. In practical water treatment applications, in addition to being biocompatible and cost-effective, the catalyst should also efficiently produce reactive oxygen species. the catalysts should efficiently produce ROS besides beginning biocompatible and cost-effective. Therefore, it is essential to seek and establish a simple and efficient singlet oxygen production system.

In recent years, metal-free conjugated polymer shows great potential in singlet oxygen generation. Considering this in mind, a famous photocatalyst g-C$_3$N$_4$ comes to our attention. As a metal-free organic conjugated photocatalyst, g-C$_3$N$_4$ has great potential for degrading

refractory organic pollutants [8–13]. g-C$_3$N$_4$ can be synthesized by the thermal polycondensation of cheap precursors [14]. g-C$_3$N$_4$ owns a suitable bandgap with great stability ability and suitable band structure, but the poor visible light absorption ability and rapid photocarriers recombination limit its application. Considering the electronic properties of phosphorus, the introduction of phosphorus into g-C$_3$N$_4$ could greatly improve the singlet oxygen production ability [15]. However, the introduction of the single active unit is not enough to make a qualitative change in photocatalytic performance. Fortunately, the highly adjustable molecular structure of g-C$_3$N$_4$ gives chances for the optimization of its photocatalytic performance. The introduction of basic active units (such as cyano group, vacancies, impurity atoms, methyl, amino, etc) during the synthesis process can effectively improve photocatalytic performance [16–18]. Nevertheless, the simultaneous introduction of multiple active units usually involves a complex preparation process, which is not conducive to manufacture [19,20]. In addition, the cooperation between the active units is also very essential, because disharmony will reduce the photocatalytic performance. Therefore, the facile method for the synthesis of multi-active unit cooperation of g-C$_3$N$_4$ is very significant.

Here, P, K-doped g-C$_3$N$_4$ with cyano group and nitrogen vacancies (PKCN) was fabricated by a facile thermal polycondensation process with the assistance of KH$_2$PO$_4$. In the thermal polycondensation process, KH$_2$PO$_4$ can provide a weakly acidic environment to promote the formation of nitrogen vacancies, and K atoms can induce the formation of cyano groups. In addition, K atoms can insert into g-C$_3$N$_4$ layers to change morphology and form electron bridges to accelerate photo-generated electron transfer. Under the synergistic effect, the singlet oxygen generation ability of PKCN was greatly improved, and greatly enhanced ATZ removal from 12% (BCN) to 83% (PK10) under visible light. Through experiments and analysis, it is proved that PKCN owns three pathways to produce singlet oxygen, which are energy transfer, hole oxidation, and dismutation reaction. When P atoms were removed from PKCN, it was found that the singlet oxygen production capacity was significantly reduced and the capacity transfer pathway was lost, indicating that P atoms play an important role in singlet oxygen production. Besides, taking an insight into the role of each active unit in the system can help to sharpen the comprehension of photocatalytic reactions. Given the complexity of g-C$_3$N$_4$ structures, the acquisition of critical roles of each molecular constituent in g-C$_3$N$_4$ for photocatalysis remains elusive. Therefore, the intrinsic mechanism and synergy of each active unit have been investigated by investigation and density functional theory (DFT). The insight into the roles and synergy of each active unit is conducive to designing and synthesizing efficient g-C$_3$N$_4$. Moreover, the probable degradation pathways of ATZ in the PK10 system were investigated through tandem mass spectrometry (LC-MS). Finally, the toxicity of intermediate products was demonstrated by the T.E.S.T. and soybean culture experiment.

2. Experimental section

2.1. Materials

The urea (99%), KH$_2$PO$_4$ (99.5%), K$_2$HPO$_4$ (AR 98%), K$_3$PO$_4$ (AR), Na$_3$PO$_4$ (AR), Na$_2$HPO$_4$ (99%), NaH$_2$PO$_4$ (99.9%), p-Benzoquinone (p-BQ, 99%), Isopropyl alcohol (IPA, AR 99.5%), Ammonium oxalate (AO, AR 99.8%), L-Histidine (L-HIS, 99%), and 9,10-Diphenylanthracene (DPA, 98%) from Macklin.

2.2. Synthesis of BCN

Urea is the precursor to synthesizing BCN via a facile thermal process. Firstly, 10 g urea was calcined at 550 ℃ (2 ℃/min) for 4 h in a 100 mL covered ceramic crucible. After cooling, the resultant solid mixture was calcined at 500 ℃ (5 ℃/min) for 2 h under an N$_2$ atmosphere to obtain BCN.

2.3. Synthesis of PKCN

The precursor of PKCN was obtained by grinding 10 g urea with different weights of KH$_2$PO$_4$. And then go through the same thermal polycondensation process as for BCN. The prepared PKCN with the addition of KH$_2$PO$_4$ dopants was labeled as PKX. Here, X represents the KH$_2$PO$_4$ dopant usage (5 mg, 10 mg, 20 mg and 30 mg).

2.4. Photocatalytic performance

The photocatalytic efficiency of the prepared samples was investigated by the degradation of ATZ under visible light. A 300 W Xe lamp (PLS-SXE 300D, Beijing Perfectlight, China) was applied as the visible light source with a 420 nm filter. First of all, 40 mg prepared photocatalytic was added into 50 mL ATZ solution (10 mg/L) and stirred in the dark for 20 min for adsorption. Then the mixture was placed on the magnetic stirrer under visible light. Upon reaction begin, the solution was collected at a specific time. The ATZ concentration of the solution was detected by high-performance liquid chromatography (HPLC). The detection wavelength was 225 nm and the mobile phase is 70% methanol and 30% ultrapure water.

The production of $^1O_2$ was detected by the loss of FFA (0.2 mM initially). The HPLC was conducted to detect the concentration of FFA. The iodine titration was applied to evaluate H$_2$O$_2$ production, detected by the UV–vis spectrometer (Shimazu UV-1700).

2.5. Soybean cultivation experiments

Details are provided in supplementary documents.

2.6. Characterization

The morphology of samples was studied on scanning electron microscopy (SEM Tescan Mira LMS with 5.0 kV scanning voltage and transmission electron microscopy (TEM FEI TalosF200x) with 200 kV scanning voltage. The pore size distribution and specific surface area were investigated via an N$_2$ adsorption-desorption isotherm (Micromeritics APSP 2460, 300 ℃ degassing). The X-ray diffraction (XRD Rigaku SmartLab SE, 5°/min scanning rate) was measured to determine the crystal structure. The Fourier transforms infrared spectrometer (FT-IR, Thermo Scientific Nicolet iS20) was used to identify the functional groups. The chemical interaction was shown by Solid-State NMR (Bruker 400 M). The chemical state of samples was conducted by X-ray photoelectron spectra (XPS, Thermo SCIENTIFIC ESCALAB 250Xi). The elemental analyzer (EA, Thermo Fisher-Flash 2000) was performed to investigate the elemental composition of samples. The chemical adsorption of O$_2$ on catalysts was studied by temperature programmed desorption (TPD Mak 2920). The light absorbance of samples was conducted by UV–vis diffused reflectance spectra (Shimadzu 3600plus). The Photoluminescence (PL) spectra and Time-resolved transient photoluminescence (TRPL) spectra were obtained by a fluorescence spectrometer (Hitachi, F-700) and Edinburgh FLS1000 respectively. The reactive species were determined by the electron spin resonance spectra (ESR Bruk) The photoelectrochemical characterization was conducted by the CHI 660D workstation. The generation of singlet oxygen ($^1O_2$) was proved by 9,10-diphenylanthracene (DPA) as chemical probes detected by the UV–vis spectrometer (Shimazu UV-1700).

3. Results and discussion

3.1. Morphology and structure analysis

Phosphorus and kalium co-doped g-C$_3$N$_4$ (PKCN) with cyano group and nitrogen deficiency was prepared by simple thermal polycondensation. The preparation and molecular structure of PKCN and BCN are shown in Fig. S1A. In Fig. S1B it was obvious that the peak

corresponding to the cyano group was increased after calcining at N_2. In addition, the peaks for P-N distributed between 980 nm emerge. Based on the above, it can be concluded that calcination under N_2 can promote the formation of the cyano group and change the chemical state of P to a more active N-P. The structures of g-C_3N_4 prepared by different precursor systems are different. The fluffy and porous structure is ideal for doping. In the thermal condensation process, urea can polymerize and release H_2O and CO_2 gas [14], leading to a more porous structure in g-C_3N_4 [21]. The porous thin section structure of BCN appeared in the SEM and TEM images (Fig. 1A-B). The loose structure is more conducive for doping because the dopant can fully contact the carrier and evenly dope. After the reaction with KH_2PO_4, PK10 samples still retain the porous thin section structure and part of them become more creased with a folded edge attributed to the warping effect of K atoms on the layer of g-C_3N_4 (Fig. 1C-D). The EDX elemental mapping of C, O, N, P, and K in the PK10 was observed in Fig. S2. The uniform element distribution indicates that KH_2PO_4 fully reacts with urea.

Upon KH_2PO_4 doping, the morphology and elemental composition have greatly changed, affecting the structure of PK10. In Fig. 1E, the specific surface areas of the catalysts decrease from 34.2 (BCN) to

23.2 m^2/g (PK10). The reduction in surface area was probably caused by KH_2PO_4 restricting the release of CO_2 gas during thermal polycondensation [22]. In addition, the porous properties of PK10 also changed after doping, which was analyzed by Barrett-Joyner-Halenda (BJH) methods (Fig. 1E). The pore diameter of BCN and PK10 was mainly distributed at 2.6 nm, indicating that mesopores were dominant in g-C_3N_4, produced by the gases released during the thermal process. Compared with BCN (0.054 cm^3/g), the PK10 exhibited a minor total pore volume (0.041 cm^3/g). Upon KH_2PO_4 doping, K atoms improve the polymerization degree of PK10, leading to an intensive pore volume. K atoms tend to constitute a bridge between the layers of PK10 for improving charge transfer. In addition, the insertion of K atoms can decrease interlayer distances, resulting in reduced specific surface areas [23]. Interestingly, the average pore size of PK10 (7.1 nm) was larger than BCN (6.4 nm). There were two possible reasons for the increase in pore size in PK10. In the first place, P atoms can insert into the heptazine of g-C_3N_4 causing structural distortion. Secondly, the plane disorder was amplified by the cyano groups and nitrogen vacancies. Both of them would produce larger size holes, thus increasing the average pore size. The thickness of the samples was estimated by atomic force microscope
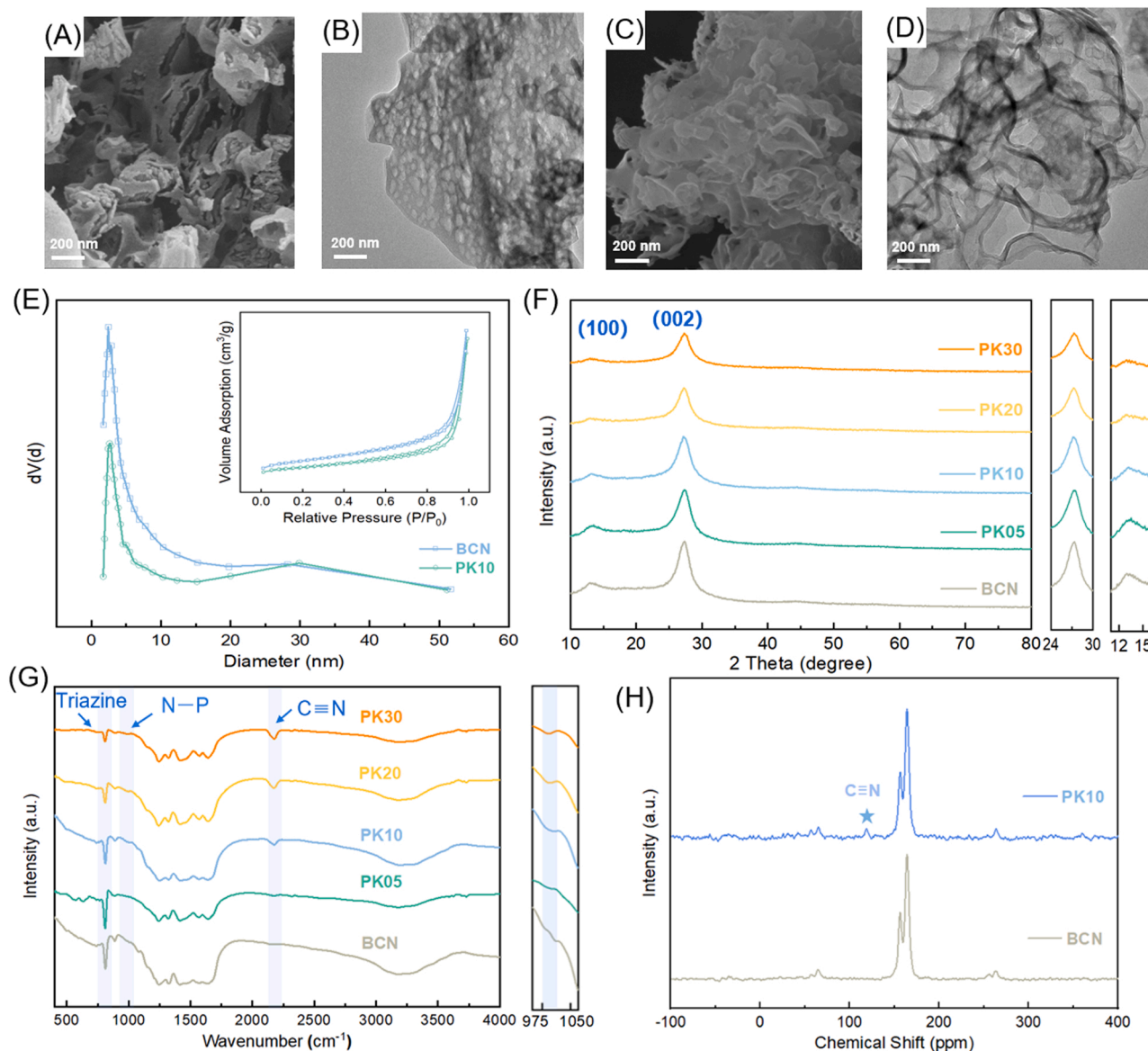
Fig. 1. SEM image of the BCN (A) and PK10 (C); TEM image of the BCN (B)and PK10 (D); (E) pore radius information and the N_2 adsorption-desorption isotherms; (F) XRD patterns and (G) FT-IR spectra of the catalysts; (H) Solid-State NMR spectra of ^{13}C.

(AFM) (Fig. S3). From this, we can see that the average thickness of the obtained PK10 was about 2 nm, slightly smaller than that of BCN (2.3 nm). This thin and porous structure facilitates the interlayer transfer of photoelectrons and promotes the separation of photoelectrons from holes.

The XRD and FT-IR spectra of PKCN were very parallel to BCN, confirming that the addition of KH_2PO_4 would not break the general framework of g-C_3N_4. Fig. 1F depicts the XRD spectra and the partial enlargement of the samples. Two characteristic peaks at around 13.2° and 27.4°, originating from the lattice planes parallel (100) and periodic stacking (002), emerged in all samples [8,24]. Both peaks widened and gradually weakened with the increase of the KH_2PO_4 doping amount, indicating that KH_2PO_4 could react with urea during the preparation process to reduce the ordered structures. In addition, the characteristic peaks shift to higher 2θ angles with increasing KH_2PO_4 usage, representing the distance of the interlayer is decreased [25,26].

The structure changes between BCN and PKX were identified by FT-IR (Fig. 1G). The peaks centered at 810 cm^{-1} are typical for the triazine ring and the peaks located between 1250 and 1800 cm^{-1} originated from the −C≡N heterocycles [27]. The gentle and broad peak distributed in the 3100–3600 cm^{-1} region is corresponding to −C−NH_2. For the PKCN samples, three obvious changes emerged in the FT-IR spectra that occurred with the augment of KH_2PO_4 usage, emphasized by blue shaded regions in Fig. 1G. Firstly, the signal peak intensity of −C−NH_2 decreased progressively related to the cyano group. Secondly, a distinct peak emerged at 2175 cm^{-1} related to the cyano group. Finally, the decreased peak intensity in the triazine ring peak centered at 810 cm^{-1}, indicating the increase of plane disorder caused by the cyano groups and nitrogen vacancies. Noticeably, a slight peak centered at 980 cm^{-1} correspond to the P − N, hinting phosphorus atoms were inserted into the heptazine of g-C_3N_4 successfully [28,29].

Besides XRD and FT-IR studies, further insight into the chemical structures of the samples was provided by solid-state ^{13}C, and ^{31}P NMR

spectra (Fig. 1H and S3C). Two strong peaks located at 156.5 ppm and 164.6 ppm can be observed in the ^{13}C spectra BCN and PK10 (Fig. 1H), which are corresponded to the C element of the framework in g-C_3N_4 [30]. Moreover, BCN and PK10 were found very parallel, indicating that the heptazine ring would not be strongly decomposed by KH_2PO_4. One new peak at 128.3 ppm emerged in the PK10, which attributes to cyano groups [31]. NMR investigations of PK10 on the ^{31}P show a weak signal between 10 and − 40 ppm (Fig. S3C) corresponded to the N-P coordinate bonds, indicating the phosphorus atom inserted in heptazine of g-C_3N_4 [29]. Thus, the N-P coordinate bonds are formed by replacing carbon in the heptazine with phosphorus [32].

3.2. Chemical compositions

To reveal the effects of KH_2PO_4 on the chemical state and element compositions of catalysts, XPS and organic elemental analysis (OEA) were performed. The proportions of C, N, and O elements of BCN and PK10 analyzed by the above methods are listed in Table S1. The O/C ratio of PK10 slightly increased than BCN, which was ascribed to the addition of KH_2PO_4 introduced oxygen species (Fig. 2 A). The N/C atomic ratios of BCN measured by OEA and XPS were 1.35 and 1.25, respectively, basically in accord with the value for g-C_3N_4 in theory [33]. Notably, the production of cyano groups is not usually accompanied by a loss of N and C in the g-C_3N_4. Nevertheless, the XPS data emerged a slight decrease in the N/C ratio for PK10 compared to BCN (from 1.25 to 1.12), indicating the information of surface N vacancies with KH_2PO_4 usage. To investigate the position and formation of N vacancies in detail, narrow scan XPS spectra for BCN and PK10 were discussed. As presented in Fig. 2B, The C 1s spectra for BCN contained three well-resolved components of N − C═N (288.2 eV), C−NH_2 (286.5 eV), and sp^2 C−C (284.8 eV). The 286.5 eV signal of PK10 was intensified compared to BCN, which was related to the cyano groups ascribing to its own the resemble binding energies to C−NH_x [34]. Moreover, the
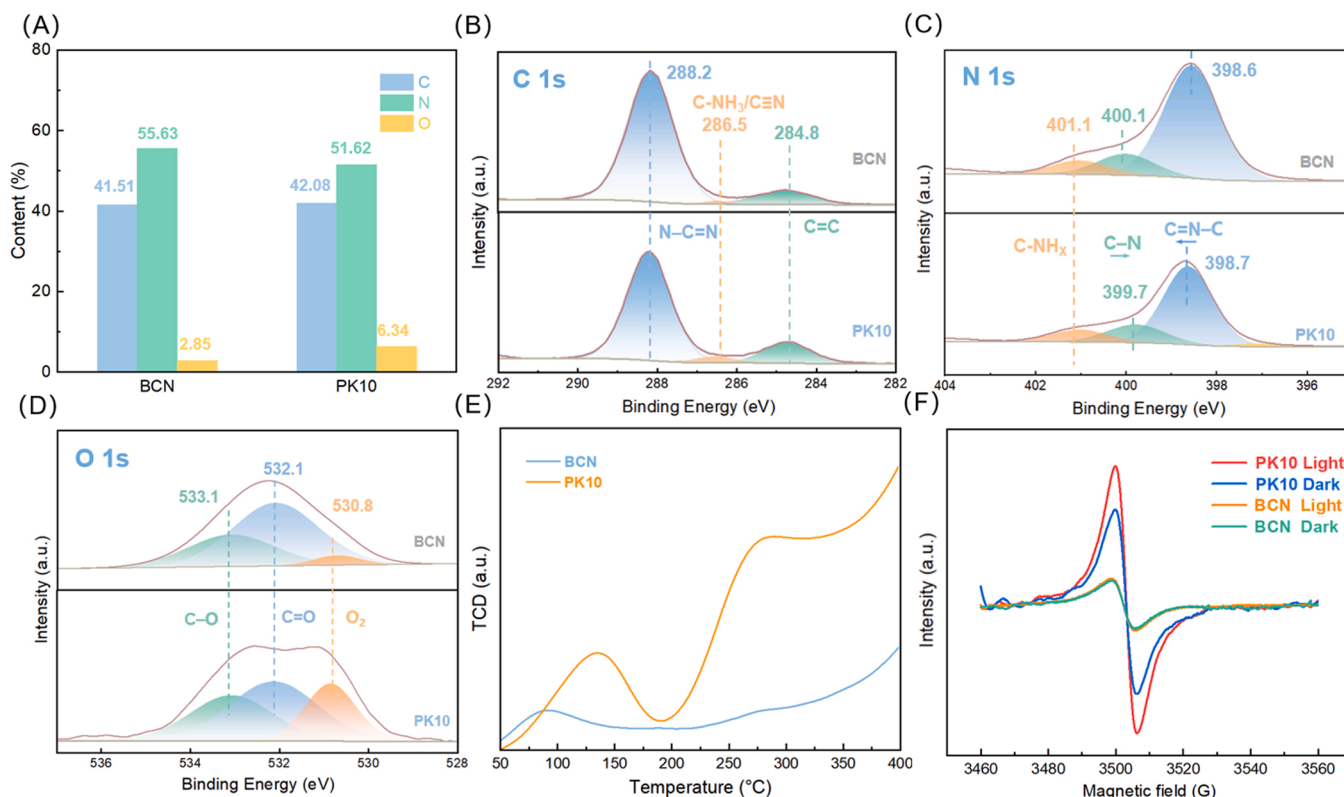
Fig. 2. (A) elemental contents; (B) the C 1 s, (C) the N 1 s and (D) the O 1 s spectra of the BCN and PK10; (E) temperature programmed desorption of O_2 on BCN and PK10; (F) EPR spectra of the PK10 and BCN.

decreased 288.2 eV signal intensity of PK10, which in company with the intensive C−NHx peak intensity could be assertive evidence for the formation of cyano groups and opening of heptazine rings (consistent with FT-IR and solid-state ^{13}C NMR). The N 1s XPS spectra for BCN possess three ingredients at 398.6, 400.1, and 401.1 eV representing sp^2-hybridized ($N_{2\,C}$), sp^3-hybridized ($N_{3\,C}$) nitrogen atoms, and NH_x groups in the structure, respectively (Fig. 2C). It is noted that the decreased 401.1 eV signal intensity of PK10 is ascribed to NH_x groups loss in the formation of cyano groups. Cyano groups are usually located at the endpoint of the g-C_3N_4 structure and derived from the conversion of −C−NH_2. After the KH_2PO_4 doping, the binding energy of $N_{3\,C}$ decreases to a lower value attributed to the cyano groups own intermediate binding energy between that of $N_{3\,C}$ and $N_{2\,C}$ [34]. Furthermore, the intensity of $N_{2\,C}$ in the PK10 significantly decreases, revealing that nitrogen vacancies were predominantly formed at the $N_{2\,C}$ position. Moreover, the binding energy of $N_{2\,C}$ in PK10 shifted to higher binding energy by about 0.1 eV, which was attributed to the N − P bond for changing the chemical environment of $N_{2\,C}$. Likewise, as shown in Fig. S4, one single peak located at 133.4 eV in the P 2p spectrum of PK10, representing the formation of the N − P bond (as shown in FT-IR) [28]. The O 1s spectra of BCN consist of O_2 (530.8 eV), C−O (533.1 eV), and C=O (532.1 eV) (Fig. 2D). After KH_2PO_4 usage, the intensity of the O_2 peak observably increased, which was attributed to oxygen absorbed on nitrogen defects. Chemisorbed oxygen can be rapidly converted to reactive oxygen species, which could accelerate the oxidative degradation of organic matter [35]. To further determine the oxygen adsorption capacity of PK10, the temperature-programmed desorption measurement was conducted. In Fig. 2E, there were two typical signals at around 80 °C and 280 °C that can be observed, representing the weak physical adsorption and the strong chemical adsorption of O_2 on catalysts, respectively. Notably, PK10 exhibits a significantly intensive TCD signal, indicating a better O_2 adsorption property than BCN. In addition, the signals of both physical adsorption and chemical adsorption shift to high temperatures, indicating that PK10 owns stronger oxygen adsorption

stability than BCN. By calculation, the physical and chemical adsorption capacity of PK10 to O_2 were 0.144 mmol/g and 0.258 mmol/g, respectively, which were 2.3 and 8.3 times of BCN. Strong oxygen adsorption ability is the crucial first step in the transition from O_2 to ROS on the catalyst.

In addition to XPS and OEA analytics, EPR further provides definite evidence for the formation of nitrogen vacancies in the PK10 (Fig. 2F). Several signals in the EPR spectra between 3460 and 3560 G. Besides, the g value was 2.004 representing the lone pair electrons of sp^2 C in the heptazine framework [32,36]. When exposed to visible light, the EPR intensity significantly intensified in PK10, indicating its strong photosensitivity and high concentration of lone pair electrons [37,38]. Above results combined with XPS and FT-IR adequately determine the successful formation of nitrogen vacancies.

3.3. Optical and photoelectrochemical properties

The diffused reflectance spectra (DRS) were performed to further investigate the bandgaps and optical absorptions of samples. The addition of KH_2PO_4 during the thermal polycondensation observably alters the absorption band and light capture ability of the samples. In Fig. 3 A, BCN emerged as a typical absorption edge distributed in the 410–440 nm region. Besides, a series of obvious redshifts of absorption edge was observed for the PKCN compared to BCN. Moreover, it is noted that PK10 shows the strongest absorption in the UV–vis region, leading to its best performance. The Kubelka-Munk function transforms from the DRS information of the catalysts [32]. As shown in Fig. 3B, the bandgap of PK10 is more marrow than BCN, revealing the superior visible light response. The VB potential (E_{VB}) of BCN and PK10 were respectively 1.77 and 1.54 eV obtained from the valence band data (Fig. S5). According to E_{VB} and E_g, the conduction band potential (E_{CB}) can be determined by calculating the following equation.

$$E_{CB} = E_{VB} - E_g$$
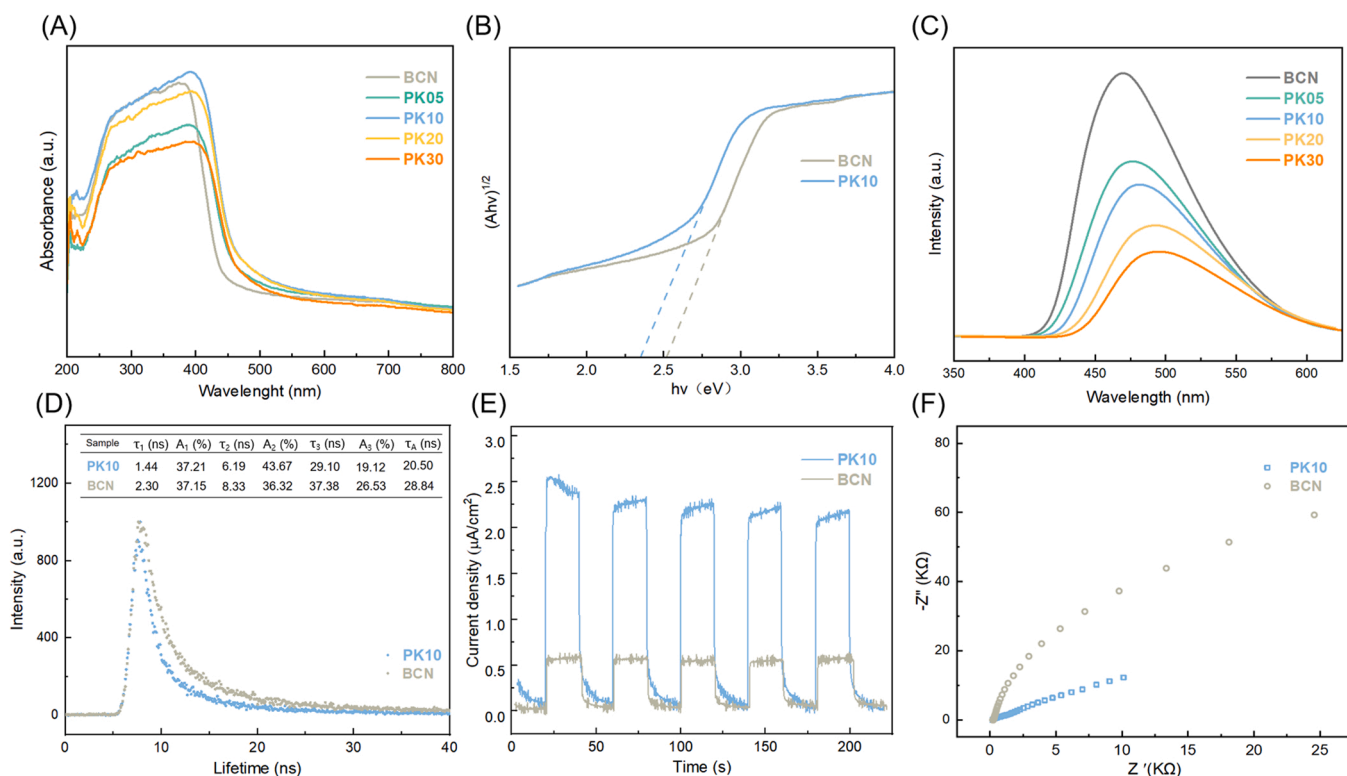
Fig. 3. (A) The DRS spectra of samples and (B) the transformed Kubelka-Munk function of the BCN and PK10; (C) PL spectra; (D) time-resolved PL decay spectra; (E) transient photocurrent response; (F) EIS Nyquist plots.

The E_{CB} of BCN and PK10 is figured out to be -0.78 and -0.81 eV respectively. In addition, the PK10 owns a more negative E_{CB} than BCN, which could lead to a greater reduction ability.

Besides the effect on the bandgap configuration, the usage of KH_2PO_4 can facilitate the separation of photoexcited carriers, evaluated by steady-state PL emission spectra and time-resolved PL decay spectra (TRPL). PL spectra of BCN and PKCN were recorded with 320 nm excitation in Fig. 3 C. BCN emerged as an intensive and wide emission signal at around 470 nm, which could be attributed to the rapid direct recombination of CB to VB [18]. After KH_2PO_4 usage, the intensity of the emission peak gradually decreases, indicating the shallow trapping of electrons inhibits charge recombination [39]. The emission peak shifts to the high wavelength with the increase of KH_2PO_4, which attributes to the electron recombination in the defect state [40]. P atoms inserted in the heptazine ring of PKCN can introduce defect states below the CB. The defect states could be an electron sink to accept the electrons that cannot reach the CB photoexcited from the VB. PKCN with the assistance of defect state can utilize the photons with less energy than bandgap, facilitating more light response [41]. Meanwhile, the defect states also receive the photoexcited electrons that relax from CB. To gain an additional understanding of the electron transfer mechanism, TRPL has been applied further to the study (Fig. 3D). The average lifetimes were determined by triexponential fitting. Consequently, PK10 (20.50 ns) exhibits a transitory average radiative lifetime than BCN (28.84 ns). The decreased lifetimes indicate more effective photocarrier formation and faster charge transfer in the PK10 [42]. It may be ascribed to the speedy radiative decay pathway of electrons induced by defect state and short transfer distance by thin nanosheet in PK10 [43]. Moreover, the transient photocurrent response was exhibited in Fig. 3E. The transient photocurrent density of PK10 was 2.4 $\mu A/cm^2$, which is 3.6 times that of BCN. The much higher photocurrent in PK10 reflects a better photocatalytic property and efficient electrons transfer [44,45]. Compared with the BCN, PK10 demonstrated a smaller impedance, which confirmed the effectively improved charge transfer (Fig. 3F).

3.4. Photocatalytic performance

3.4.1. Photocatalytic atrazine degradation

The removal of ATZ was used as an indicator of the photocatalytic performance of samples. Fig. 4 A and E exhibited the removal and reaction rate constants of ATZ by the PKCN with different KH_2PO_4 doping amounts. Only 14% of ATZ can be removed by BCN under visible light. All PKCN emerged with remarkable enhanced efficiency in ATZ degradation compared with BCN, although BCN owns a higher specific surface area. The specific surface area can affect photocatalytic performance but is not the decisive factor. It could be attributed to other modification properties induced by KH_2PO_4. The electron transfer behavior and catalyst properties also have significant effects on photocatalytic performance. PK10 emerged with the most excellent degradation performance, with an 83% ATZ degradation rate (k = 0.0278 min^{-1}). This result indicated that the PK10 exhibited dominant advantages in ATZ degradation attributed to the incorporation of KH_2PO_4. However, with the increasing usage of KH_2PO_4, the performance of PKCN for ATZ degradation decreased gradually, which may be ascribed to excessive KH_2PO_4 usage that destroys effective photocatalytic structural units and introduce redundant active sites resulting in recombination of photogenerated carriers [46]. Since PK10 owns the best ATZ degradation performance, the PK10 was used in the following experiments. Besides, the effect of catalyst dosage on degradation was studied (Fig. 4B). It can be found that 0.8 g/L is the best dosage. Less dosage is not enough for full reaction, and excessive dosage will lead to the reduction of light transmission capacity.

The initial pH value of the system has a significant effect on reaction activity because it can influence the formation of ROS. Therefore, the ATZ degradation performance of PK10 and BCN was assessed under pH= 3 ~11 (Fig. 4 C). The PK10 showed excellent efficiency in an acidic and neutral environment (pH= 3~7), especially the photocatalytic ATZ removal even reached 95% at pH= 5 (K=0.051 min^{-1}). The better degradation performance can be attributed to the easier generation of active species in an acidic environment. According to ZETA potential
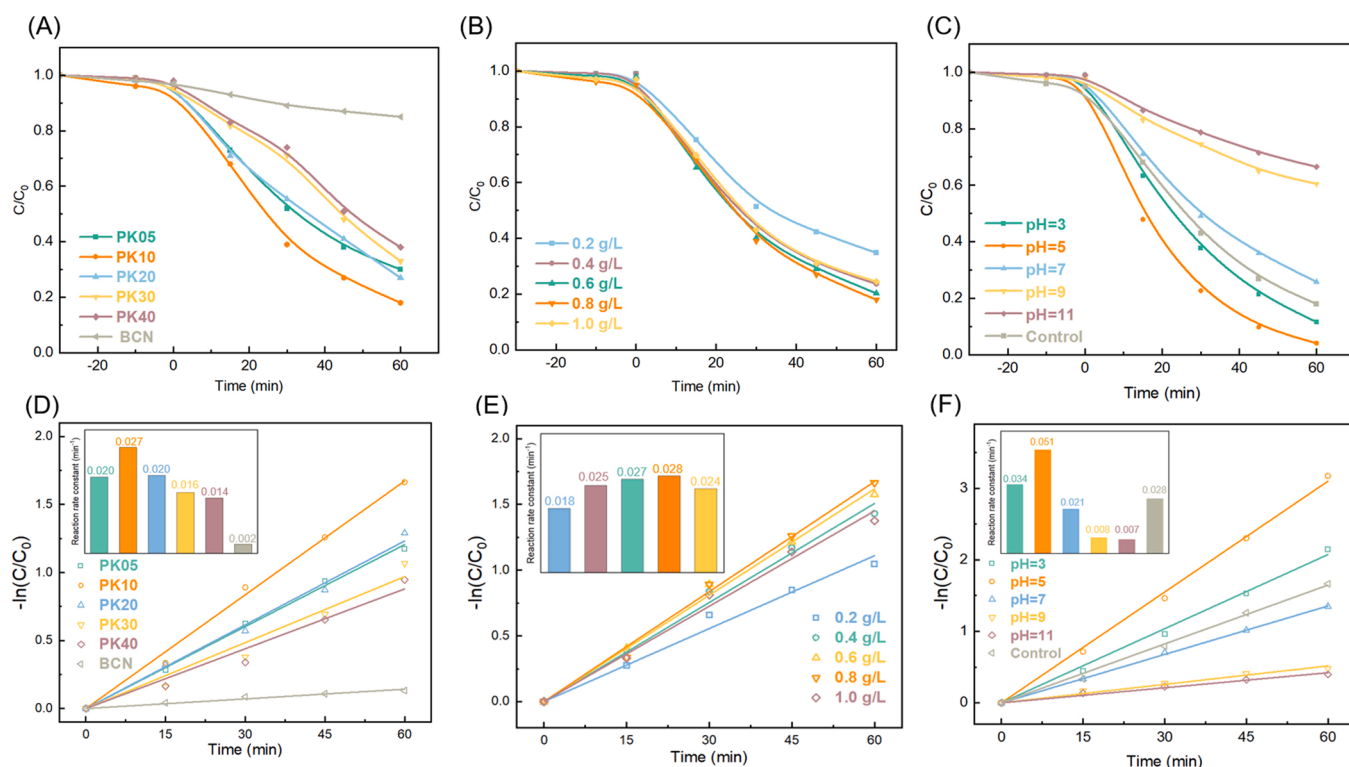
Fig. 4. (A) the removal of ATZ by PKCN with different KH_2PO_4 usage; (B) the photocatalytic catalytic performance of different PK10 dosages; (C) the effect of initial pH on ATZ removal for PK10; (D-F) the pseudo-first-order Kinetic plots of (A), (B), and (C) respectively.

(Fig. S6), the PK10 surface was positively charged in a weakly acidic environment. The ATZ exhibited negative potential ascribed to the ionization of NH groups, improving its adsorption on PK10. However, when the pH value was approaching the pKa (pH=2), ATZ will protonate and become cationic form. The removal rate slightly dropped to 87% (K=0.031 min^{-1}) which ascribed to ATZ being protonated in a strong acid environment (pH=3), inhibiting the absorption of ATZ on PK10 [47]. The photocatalytic efficiency decreased with the increase of pH, and the ATZ removal rate decreased to 35% (K=0.007 min^{-1}) with pH= 11. In an alkaline system, the electrostatic repulsion impeded the degradation of ATZ. The ATZ mineralization extent in this system was further assessed via the TOC analysis (Table S2). As shown in Table S2, the TOC of the initial solution of ATZ is 10.71 mg/L, while the after-reaction solution is 3.53 mg/L. the After 60-min photocatalysis, the solution TOC content significantly decreased to only 32.9% of the 10 mg/L ATZ, achieving a 67.1% TOC removal rate.

3.4.2. The study of different dopants

The photocatalytic capacity of the doped catalyst is significantly decided by the properties of dopants because the attributes of the catalyst are determined by the interaction between the dopant and the precursor. Phosphates other than KH_2PO_4 were employed as substitute dopants to systematically discuss the cationic and properties effects on the PKCN to degrade ATZ. The same mole amounts of phosphates as the PK10 were utilized as dopants, including NaH_2PO_4, Na_2HPO_4, Na_3PO_4, K_2HPO_4, and K_3PO_4. The degradation and reaction rate constants of ATZ by the catalyst with different kinds of dopants were displayed in Fig. 5A-B. The melting point of dopant plays a decisive role in thermal condensation. In Fig. 5 C, the melting point of each substance can be observed. It can be found that NaH_2PO_4 and Na_3PO_4 own too low melting points not conducive to doping. In addition to the low melting points, the boiling points of NaH_2PO_4 (100 °C) and Na_3PO_4 (158 °C) are also too low and would turn into gases in the reaction system, resulting in insufficient contact with urea. Moreover, the high melting point of

K_3PO_4 makes it solid during the whole process of thermal process, which was also not conducive to doping. When heated to 204 °C, K_2HPO_4 will undergo internal dehydration and convert to potassium pyrophosphate. Therefore, KH_2PO_4 becomes a suitable dopant because of its appropriate melting points and property. Moreover, when acidic KH_2PO_4 and NaH_2PO_4 were mixed with alkaline urea, the interaction between them was enhanced by acid-base neutralization during thermal poly-condensation. This is the reason why the catalyst prepared by NaH_2PO_4 is more effective than that prepared by Na_2HPO_4, even though Na_2HPO_4 has a more suitable melting point. The photocatalytic performance of the KH_2PO_4 doped catalyst is better than that of NaH_2PO_4, which is probably because the suitable melting points of KH_2PO_4 and the doping mode of K atoms is different from that of Na atoms [47]. To sum up, the suitable properties of KH_2PO_4 together contribute to the efficient photocatalytic ATZ degradation performance of PK10.

3.4.3. Absorption and utilization of light

Based on the Beer-Lambert law: A= -lg (I/I$_0$)= εbc (A: absorbance, I: transmitted light intensity, I$_0$: incident light intensity, ε: extinction coefficient, b: optical path length, and c: concentration of light-absorbing substance). Therefore, the extinction coefficient of prepared photocatalysts can be calculated by the following formula: ε = A/(bc). The absorbance of the prepared catalysts in water suspension is exhibited in Fig. S7. According to the average absorbance of the prepared catalysts, the average extinction coefficients can be obtained (detailed data in Table S3). It can be found that the BCN possesses a high absorbance than various PKCN. The high absorbance of BCN is related to its structure. According to the results of TEM, SEM, and AFM, it is obvious that BCN possesses a fluffier and thicker structure than PK10. The fluffier structure can reduce light scattering and thereby improves light absorption. In addition, thinner structures own high light transmissivity, leading to lower absorbance. Besides, the absorbance of the PKCN prepared with different dopants is measured. It is obvious that the PKCN prepared with Na_3PO_4 and Na_2HPO_4 show a remarkably intensive absorbance than
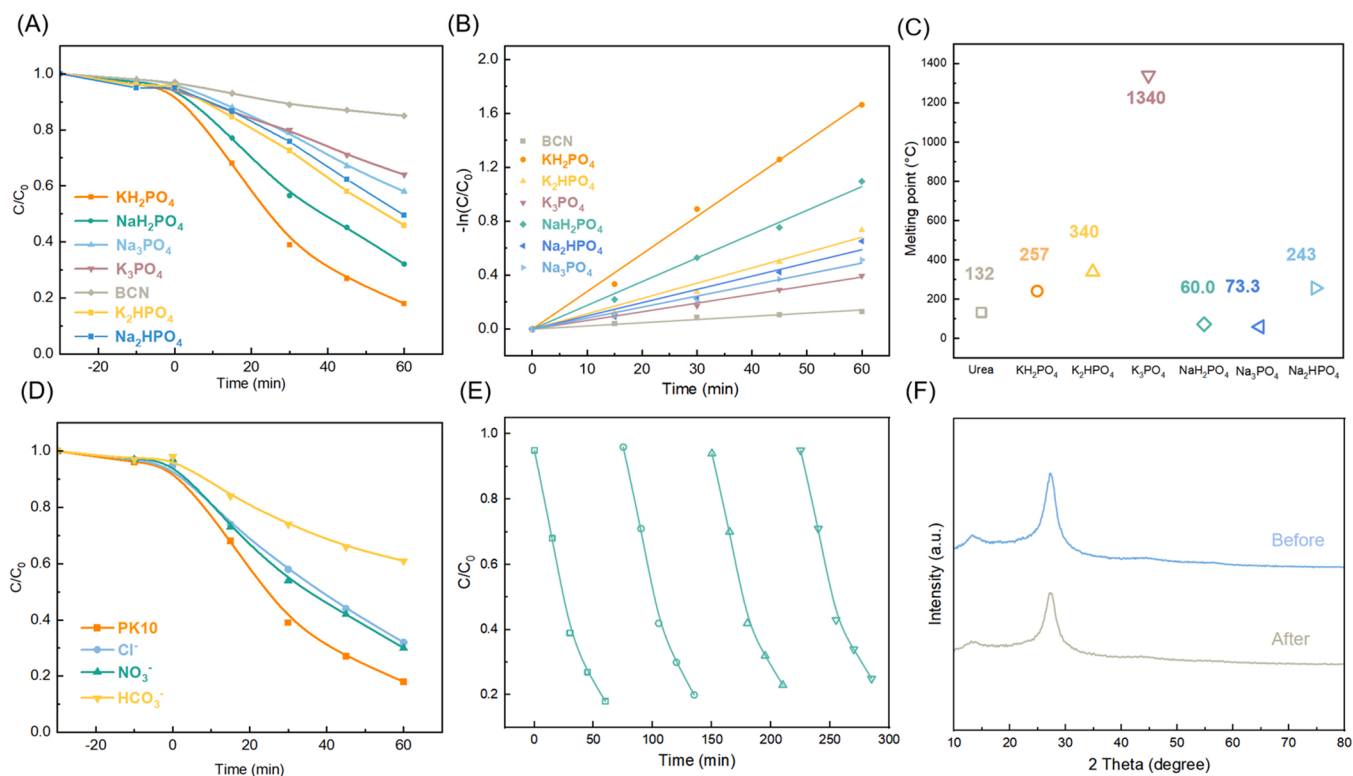
Fig. 5. (A) the photocatalytic performance of catalysts with different dopants; (B) the pseudo-first-order Kinetic plots; (C) the melting point of the dopants; (D) the effect of coexisting ions on the reaction; (E) the cycling experiment of the PK10; (F) XRD spectra comparison of the PK10 before and after use.

others, attributed to their darker yellow color. Moreover, it can be found that the average extinction coefficients of PK05-PK30 decrease gradually with the increase in doping amount, indicating that excessive doping will reduce the light absorption ability of the catalyst. Unexpectedly, the catalyst prepared with Na_3PO_4 has a higher absorbance average extinction coefficient than PK10, while the photocatalytic performance of PK10 is significantly higher than that of Na_3PO_4-prepared. It might attribute to PK10 having better utilization of light. These indicate that light absorption is not the only factor affecting photocatalytic performance, but the effective utilization of light also has a significant impact on photocatalytic performance.

The optical thickness (τ) of the prepared catalyst is significantly related to the photon absorption efficiency. According to the previous study, the optimum range of τ in the photocatalytic system was 1.8–4.4 [48]. The τ of the catalyst suspension can be calculated by the following formula: τ = h × C × ε; (h: the depth of liquid in the reactor; C: the catalyst concentration; the average extinction coefficient) [49,50]. When the amount of catalyst is the same (0.8 g/L), PK10 has the strongest photocatalytic performance than another catalyst. The suitable optical thickness of the reaction system is 2.05 of PK10 (0.8 g/L). In addition, the optimal usage of PK10 is also 0.8 g/L. Therefore, the optical thickness (2.05) of PK10 (0.8 g/L) can be identified as the best value that is used in the experiments. According to the average absorbance, the average transmittance can be calculated by the following formula: A= - log T. The transmittance can indirectly reflect the ability of the catalyst to absorb radiation. The radiation power of a 300 W xenon lamp is about 550 W/m^2. According to the transmittance data, the absorbed radiation of each catalyst can be obtained. The detailed data of transmittance are shown in Table S4. Each catalyst absorbs different radiation under the same usage, which would affect the comparison of photocatalytic performance between catalysts. Therefore, it is necessary to perform experiments at an equal optical thickness to make a meaningful comparison between the photocatalysts. To obtain equal optical thickness, the usage of each catalyst is calculated by average extinction coefficients. The ATZ degradation by different catalysts with equal optical thickness is shown in Fig. S8. It is obvious that the PK10 still exhibits the best ATZ degradation efficiency. The PK10 exhibited the best ATZ degradation under the same amount and optical thickness respectively, which is sufficient to fully prove that PK10 had the best photocatalytic performance.

Good light absorption is not always accompanied by good photocatalytic efficiency. Effective utilization of photons is the main factor affecting photocatalytic performance. The quantum yield of fluorescence (QY) measurement was conducted to reflect the total rate of photon absorption. QY is the ratio of the excited state photon to the incident photon. The excited state photon can participate in the reaction, thus the QY is significantly related to the photocatalytic performance. As shown in Fig. S9, PK10 and BCN exhibit different intensities of fluorescence under the excitation of light 310–330 nm light. After software calculation, it can be concluded that the QY of BCN and PK10 is 0.642% and 3.28% respectively. Obviously, the PK10 has a large QY, which can effectively improve the utilization of light energy. Even though BCN has a larger extinction coefficient, PK10 has a stronger photocatalytic performance, which is attributed to the higher QY of PK. Therefore, making photocatalysts use photons more efficiently is an important step to improve photocatalytic performance.

3.4.4. Practicality assessment of the PKCN

Except for the factors mentioned above, more interference factors affect the degradation performance in a practical environment. To appraise the practicality of the PK10, a series of environment factor experiments were conducted. Many ions of the environment would affect photocatalytic performance, thereby the effect of coexisting ions was evaluated (Fig. 5D). The addition concentrations of each ion were 0.05 M. The photocatalytic degradation efficiency was slightly declined with Cl$^-$, NO$_3^-$ existing. specifically, HCO$_3^-$ greatly suppressed the ATZ

degradation to only 38%. This inhibition effect is due to the alkaline nature of the reaction system caused by the hydrolysis of HCO$_3^-$. To further evaluate the practicality of PKCN, different types of pollutants to test the performance of the PK10 (Fig. S10A), such as antibiotics (Ciprofloxacin 40 mg/L), pesticides (Dinotefuran 10 mg/L and Nitenpyram 20 mg/L), and painkillers (Ibuprofen 10 mg/L). It can be found that PK10 exhibit a good degradation efficiency for all pollutants within 60 min. In addition, the ATZ degradation experiments are carried out under real water conditions. The pH value of the filtered river water (collected from Liu yang River) is 6.94. The ATZ removal in river water is decreased to 64% within 60 min. When the river water prepared ATZ solution is adjusted to pH= 5.04, the ATZ removal can recover to 78%, indicating that the PKCN owns great practicability (Fig. S10B).

The ability to reuse is an essential characteristic of the photocatalyst. The stability of the samples was assessed through repeated reactions. In Fig. 5E, after running four times, the ATZ degradation performance in the photocatalytic system is stable, decreasing from 83% to 75%. In addition, XRD and XPS were carried out to access the stability of PK10. The XRD spectra comparison of PK10 before and after use is shown in Fig. 5 F. The peaks of PK10 were retained, with the intensity of the 27.4° peak slightly decreased. It indicates that the structure of PK10 remains intact after four times of utilization. The XPS was used to determine whether the active sites were changed (Fig. S11). Compared with the fresh PK10, the positions of peaks were almost unchanged. The characteristic peak signal representing the cyano groups can be found. Based on the above, PK10 owns great practicality on ATZ degradation. In addition, the photocatalytic ATZ degradation performance compared with other state-of-the-art catalysts were listed in Table S5.

3.5. Reaction mechanism study

3.5.1. Reactive substance analysis

To determine the ROS in the system for ATZ degradation, 1,4-Benzoquinone (p-BQ), furfuryl alcohol (FFA), ammonium oxalate (AO), and isopropanol (IPA) were applied to quench ●O_2^-, $^1O_2$, h$^+$ and ·OH, respectively (Fig. 6A) [28,35]. It was found that when 2 mM IPA was added to the reaction system, the ATZ degradation was slightly inhibited to 70% removal, indicating that ● OH exhibited little contribution to ATZ degradation. Comparatively, both p-BQ and AO have a great influence on ATZ degradation. When 2 mM p-BQ and AO were appended to the system respectively, the degradation effect decreased to 20% and 37%. To a surprise, FFA had the strongest inhibition on photocatalytic ATZ degradation. It was ATZ removal rate that was significantly reduced to 5% with only 1 mM FFA applied. The result indicates that $^1O_2$ species were the main force of the degradation process.
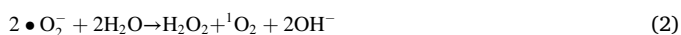
To exactly investigate the ROS generated by PK10, ESR spin-trap measurement was implemented under visible light (Fig. 6D-F). Obviously, there were no signals emerged in the darkness, while the clear signals for ● O_2^-, $^1O_2$, and ●OH can be detected at the 10 min irradiation. The results of ESR demonstrated that reactive species were produced by PK10. To further detect the formation of $^1O_2$, the DPA act as a chemical probe to identify $^1O_2$ [51]. The $^1O_2$ could react with DPA to generate the indicative endoperoxide (DPAO$_2$), resulting in a decrease in absorbance. Considering ethanol (EA) may limit the photocatalytic performance of PK10, the reaction system is 50 μmol/L DPA solution (EA: H$_2$O= 1:1). As shown in Fig. S12A, it can be found that DPA maintains a stable absorbance after 1 min visible light irradiation. When PK10 is applied in the reaction system, the absorbance exhibits a significant decrease within 15 s. Singlet oxygen possesses a short lifetime in H$_2$O, while it increases significantly in D$_2$O. It is obvious that the decrease of absorbance in D$_2$O is stronger than in H$_2$O (Fig. S12B). Thus, these can identify the formation of $^1O_2$. However, considering the band configuration of the PK10, the ·OH could not be generated directly because the E$_{VB}$ of PK10 falls short of the potential of ●OH/OH$^-$ (1.99 eV), which is discordant with the results of ESR [52]. This indicates that there is
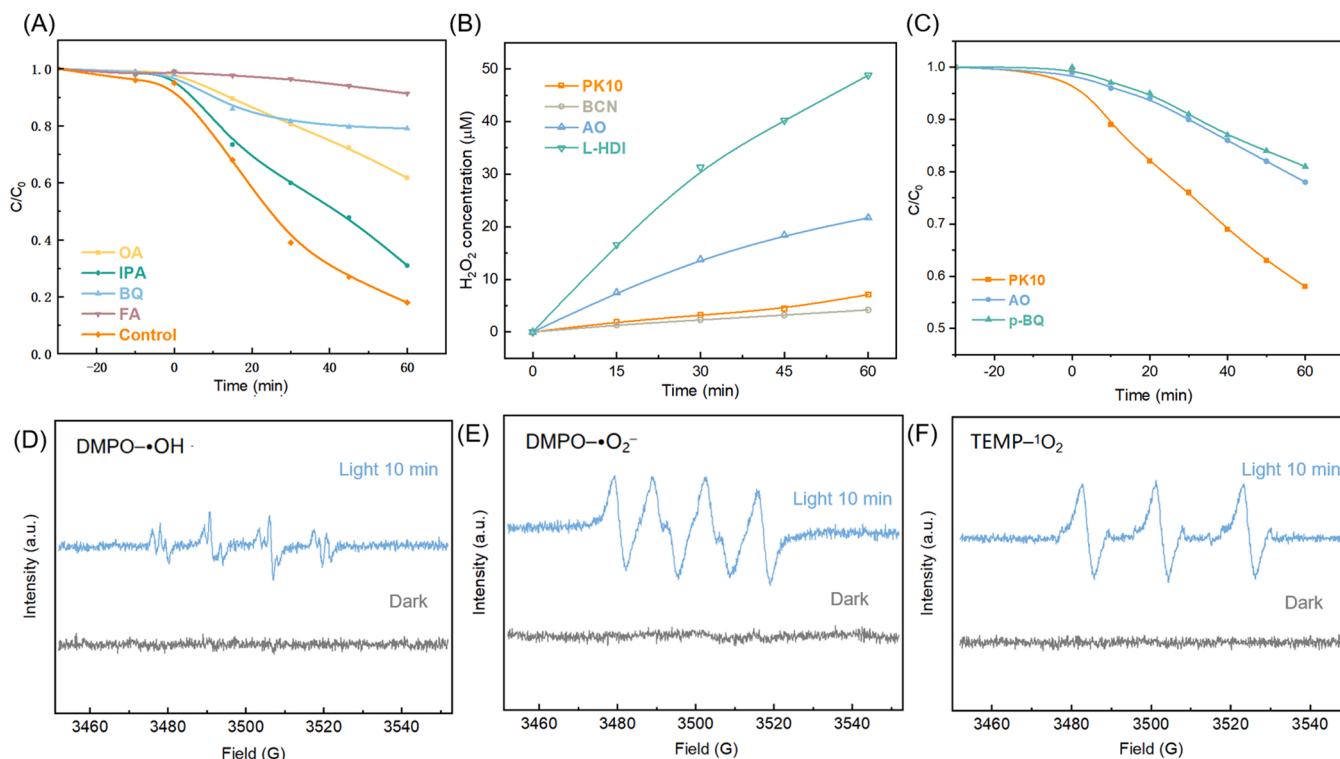
Fig. 6. (A) the degradation of ATZ with different ROS scavengers; (B) the photocatalytic H_2O_2 generation with different ROS scavengers; (C) removal of FFA on PK10 by scavenging different ROS; the ESR results of $\bullet OH$ (D), $\bullet O_2^-$ (E) and $^1O_2$ (F) in the darkness and visible light irradiation.

another path generation for $\cdot OH$. In general, H_2O_2 is formed through the reduction of O_2 on CB and produces $\bullet OH$ [53]. In addition, the E_{CB} of PK10 satisfies the condition of producing H_2O_2 (O_2/H_2O_2 0.69 eV), indicating PK10 owns the ability to generate H_2O_2. Moreover, $\bullet O_2^-$ could participate in H_2O_2 production through the dismutation reaction [54,55].

$$O_2 + 2H^+ + 2e^- \rightarrow H_2O_2 \tag{1}$$

$$2 \bullet O_2^- + 2H_2O \rightarrow H_2O_2 + {}^1O_2 + 2OH^- \tag{2}$$

$$H_2O_2 + e^- \rightarrow \bullet OH + OH^- \tag{3}$$

Therefore, to investigate the pathway of $\bullet OH$ generation, the production of H_2O_2 was monitored (Fig. 6B). Under visible light irradiation, PK10 exhibits slightly increased H_2O_2 production than BCN. Notable, when 2 mM AO was added to the PK10 system, the production of H_2O_2 had been increased 4 times. Usually, in this case, the h^+ scavenger can promote the photoexcited-carriers separation, resulting in many e^- reacting with oxygen to produce H_2O_2. [56]. In addition, when 2 mM L-Histidine was added to the system, the same situation occurred as with AO, in which the yield of H_2O_2 was increased to 10 times. Hence, H_2O_2 production from PK10 might be derived from the disproportionation reaction of $\bullet O_2^-$. Meanwhile, it was a pathway for singlet oxygen production.

Further analysis of the pathway of $^1O_2$ could provide comprehension of the degradation reaction of PK10. According to vast studies, $^1O_2$ can be formed by an energy transfer pathway or oxidation reaction process [57]. The O_2 obtains energy from the catalyst and transfers to $^1O_2$ is the common pathway, accompanying the appearance of phosphorescence (PH) [58]. In Fig. S13A, the steady-state PH spectra of PK10 emerged with an obvious peak at 480 nm, confirming the existence of an energy transfer pathway. Inversely, the PH signal cannot be observed in the BCN. In addition, the formation of $^1O_2$ is also accompanied by fluorescence in the near-infrared region [59]. In the near-infrared PL spectra,

three obvious peaks emerged (Fig. S13B). The two weak peaks of PK10 in the 980 nm attachment were associated with nitrogen vacancies and an impurity state [60]. The intensive peak located at 1200 nm corresponds to the fluorescence emitted during energy transfer to form $^1O_2$ [61]. However, none of the above phenomena was observed in the BCN, indicating that the ability of PK10 to generate $^1O_2$ through the energy transfer pathway was greatly improved after KH_2PO_4 usage. Furthermore, FFA is broadly used for determining the $^1O_2$ production because of its high reactivity to $^1O_2$ [62]. To further identify the pathway for $^1O_2$ productions PK10, discussed the effect of $\bullet O_2^-$ and h^+ on the production of $^1O_2$. If the generation of $^1O_2$ is principally by the energy transfer pathway, the presence of $\bullet O_2^-$ and h^+ scavenger will not inhibit FFA removal efficiency. Therefore, FFA removal experiments were carried out in different ROS scavengers (Fig. 6C). The 0.5 mM FFA was removed by PK10. It was found that when 2 mM AO was applied to the system, the FFA removal rate was reduced from 43% to 22%. This result indicated that the removal of FFA was inhibited in the presence of AO and the direct energy transfer might not be the predominant pathway. This phenomenon might occur due to AO inhibits the oxidation reaction of $\bullet O_2^-$ by consuming h^+ [63]. With the presence of 1 mM p-BQ in the reaction system, the loss of FFA is also impeded remarkably. Therefore, it was conjected that $^1O_2$ was mainly produced from the oxidation of $\bullet O_2^-$ by h^+ on PK10 Eq. (4). Based on the above analysis, the pathways of singlet oxygen formation in PK10 have been identified as hole oxidation, energy transfer, and dismutation reaction respectively, in which the hole oxidation is the main pathway. The PK10 has achieved outstanding $^1O_2$ production capacity under the synergetic action of four components. However, which specific component plays a crucial role in PK10 is not clear.

$$O_2^- + h^+ \rightarrow {}^1O_2 \tag{4}$$

Therefore, annealing at 500 °C in the air to eliminate P atoms to form KC10, and found that the ability of the $^1O_2$ generation has been greatly diminished (Fig. 7A). To determine the structure of KC10, XPS and FT-IR
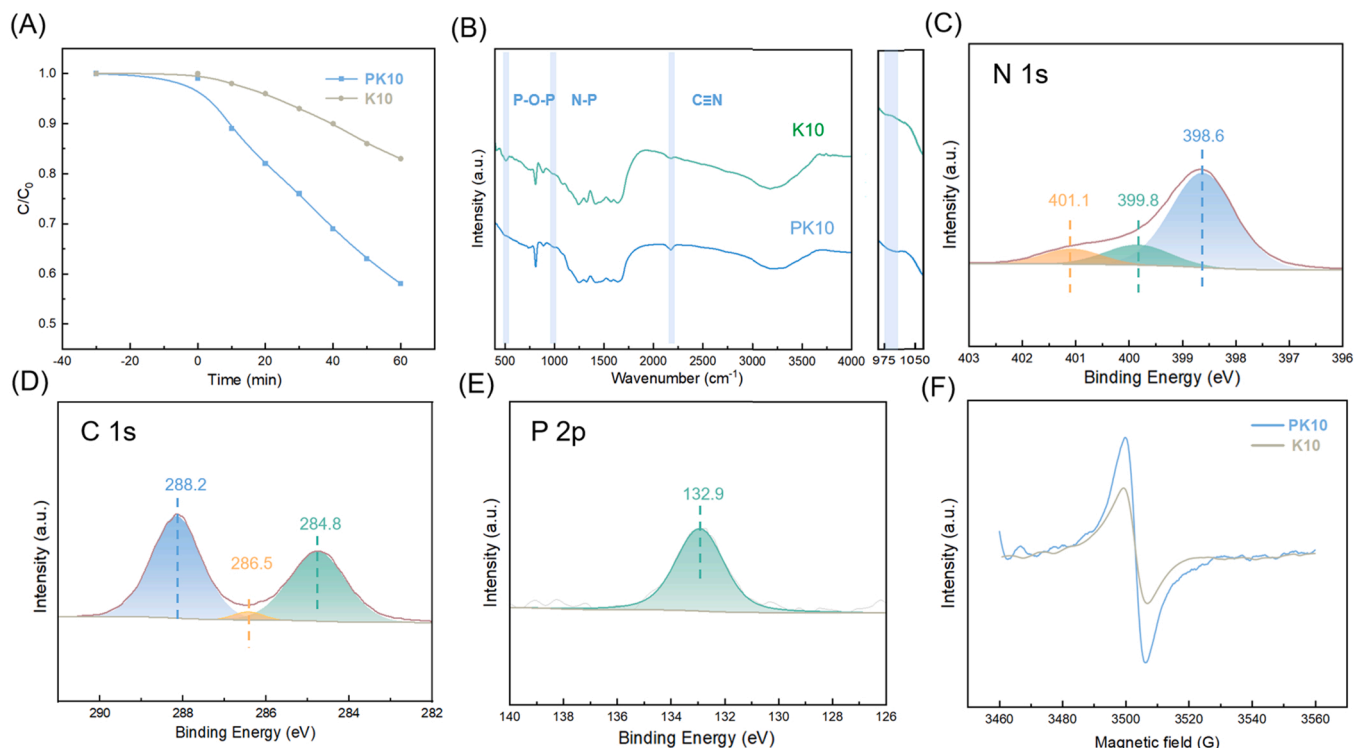
Fig. 7. (A) loss of FFA on PK10 and K10; (B) FT-IR spectra of PK10 and K10; (C) the N 1s, (D) the C 1s, and (E) the P 2p spectra of the K10. (F) EPR spectra of PK10 and K10;.

measurements were performed. In FT-IR spectra (Fig. 7B), the typical signal of the cyano group can be observed in KC10, but the signal representing N-P bonds disappeared. In addition, a strong peak emerged at 490 cm^{-1}, representing P-O-P bending modes. It indicates that the P atoms were stripped from the heptazine of PK10. The results of XPS further support this conclusion (Fig. 7C-E). In the P 2p spectra, one peak located at 132.9 eV corresponded to P-O, which is different from PK10 [64]. In addition, the intensity of the 288.2 eV peak representing N − C≡N in heptazine was decreased, ascribed to heptazine destruction caused by the stripping of P atoms. Moreover, the typical signal representing the cyano group can still be observed in N 1s spectra, and The N$_{2C}$ offset caused by N − P also disappeared. EPR experiments were conducted to detect the nitrogen vacancies in KCN-10 (Fig. 7F). It was found that the signal representing nitrogen vacancies appeared in EPR spectra but the intensity was slightly lower than that of PK10. Besides, in the near-infrared PL spectra, the signal representing singlet oxygen disappeared, indicating KC10 has lost the energy transfer pathway for singlet oxygen production (Fig. S13C).

It can be inferred that the ability of PK10 to produce singlet oxygen will be greatly reduced after the loss of P atoms because KCN-10 still has cyano groups, nitrogen vacancies, and K atoms. It is possible to hypothesize that P atoms might be the potential singlet oxygen active sites. Moreover, the efficient singlet oxygen generation ability of PK10 might be attributed to the synergies between the active components. To reveal the synergy between active components, the density of functional theory (DFT) was conducted.
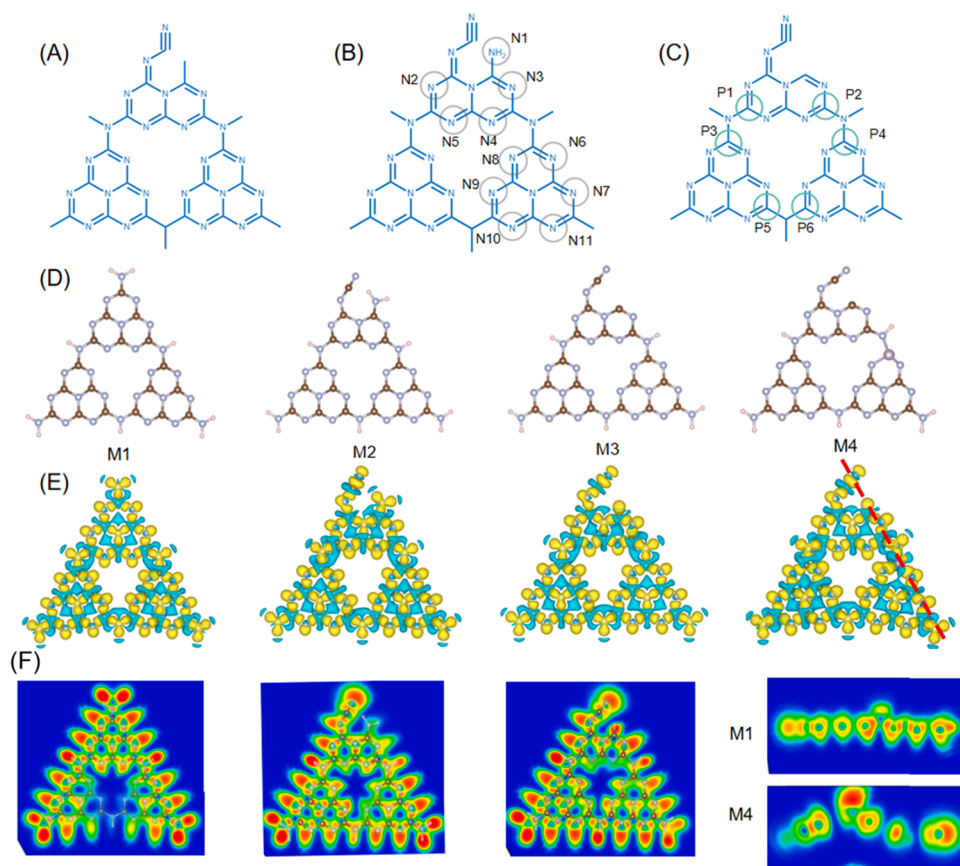
3.6. Reveal synergy of active components

Efficient photocatalytic performance is determined by the synergy between various factors, including photogeneration charges separation and transfer efficiency, surface oxygen adsorption, and electronic structure. To understand the synergy between components, one must first understand the role of each component. The structure of PK10 needs to be determined to investigate the synergy of the components

accurately. The position of the cyano is relatively permanent because the cyano group is converted from −NH$_2$ at the edge of the heptazine of PK10 (Fig. 8A). Based on previous XPS analysis, there are eleven possible formation positions for nitrogen-vacancy in PK10. In Fig. 8B, the formation energy (E$_f$) determined from DFT exhibits that the nitrogen-vacancy in the N1 position owns the lowest E$_f$. According to the previous analysis, the carbon would be replaced by phosphorus heteroatoms to form the N-P bond in the PK10 framework (Fig. 8C), and find P4 is the preferable structure by calculation. Therefore, the optimal PK10 crystal structure is shown in Fig. 8D.

First of all, the structure of the photocatalyst owns a significant effect on photocatalytic performance because the reaction usually happens on the surface [47]. The K atoms will cause such a drastic change in the model of g-C$_3$N$_4$ that it should be analyzed separately. Based on previous studies, K atoms tend to be inserted into g-C$_3$N$_4$ between layers [5]. After optimization, the structures of the K intercalated and pristine model were exhibited in Fig. S14. Obviously, K atom intercalation distorts the plane structure of g-C$_3$N$_4$, causing a significant reduction in the interlayer distance. This leads to a thinner structure, which coincides with the result of TEM and AFM. The decreased interlayer space in the g-C$_3$N$_4$ is possible to enhance interlayer electron migration and thereby improve the transfer [65]. The intercalated K connect with adjacent layers to form the electronic bridge, optimizing the transfer route and improving the separation capacity of charges. Due to the unique electronic mechanism of K, electron delocalization and the π conjugate system can be increased. In addition, the frame of each model was not significantly varied by the cyano group, nitrogen vacancies, and P atoms.

Moreover, the charge distribution of photocatalytic materials can induce an internal electric field and thus affect electron transfer. The electrostatic potential (ESP) map was calculated with the VASP software package (Fig. 8E). With no doubt, the absolute symmetrical structure of M1 was inevitably accompanied by uniform charge distribution. The uniform charge distribution is unfavorable to the separation of photoexcited carriers thus leading to rapid recombination. Meanwhile, it is difficult to ensure the effective utilization of photogenerated electrons

without the impel of the internal electric field. As a strongly electro-negative group, the introduction of the cyano group will break the previous charge balance. Obviously, the cyano group was surrounded by an area of charge accumulation in Fig. 8 F. As well as, the introduction of nitrogen vacancies and P atoms further disrupts the charge balance (Fig. 8F). The internal electric field is successfully formed by the apparent uneven distribution of charge. [66]. The directional transfer of photogenerated charges driven by the internal electric field will improve the separation and utilization efficiency.

Besides, according to the previous analysis, the ROS in the reaction system was transformed from oxygen. Therefore, the capacity of oxygen adsorbed by catalysts plays an essential role in photocatalytic perfor-mance, and superior oxygen adsorption capacity can greatly improve the generation of ROS. To investigate the role of adsorbed oxygen in the reaction process, The ATZ degradation is performed under N$_2$ purge to remove the O$_2$ (Fig. S15). It can be found that the removal of ATZ de-creases to 40% from 83%. N$_2$ purging can restrict the catalyst from trapping oxygen in the air. Under N$_2$ purging, ATZ degradation mainly is attributed to the ROS transformed from the O$_2$ adsorbed by nitrogen deficiency before the reaction start. Therefore, the adsorbed oxygen can speed up the reaction. It has been proved that PK10 has a stronger ox-ygen adsorption capacity than BCN through XPS and TPD analysis, but the specific mechanism is not clear. To clarify the mechanism, the adsorption behavior of oxygen on the models with the different active units was investigated by DFT visualization. As shown in Fig. 9A, it was found that the oxygen adsorbs feebly to M1 and M2 accompanied by weak charge transfer, in contrast, M3 and M4 own strong adsorption and conspicuous electron transfer. About M3, an evident electron link occurs around nitrogen vacancies and oxygen thereby the oxygen can be acti-vated. The oxygen on M3 (1.381 Å) owned a larger length than M1 (1.244 Å), which facilitated bond breakage and activation. Moreover, the calculated ΔE_{ads} of the oxygen on M3 increased from 0.049 eV to

3.35 eV compared to M1. In addition to the significant increase in ΔE_{ads}, the electron transfer of M3 (Δq= 0.75 e) between oxygen is also much stronger than M1 (Δq= 0.08 e). In addition, the introduction of the cyano group and P atoms has no significant effect on oxygen adsorption.

In addition, the electrostatic potential affects photoinduced electron transfer. The visualize charge distribution is displayed in Fig. 9B. Notably, the CBM and VBM in the M1 model show a prominent sym-metry and the excessive overlap of the electrons and holes leads to rapid recombination. Evidently, after the introduction of cyano, the charge distribution changed dramatically. It was found that CBM was concen-trated around the cyano group, while VBM is away from it. The intro-duction of nitrogen vacancies further amplifies the asymmetrical distribution. Notably, there was a very strong CBM aggregation area around the P atom, indicating that the introduction of the P atom remarkably affected the photoinduced electron transfer. To investigate the electronic band configuration of models, the total and partial density of states were obtained by DFT calculation (Fig. 9C-D and S16). Generally speaking, the calculated bandgaps are usually inconsistent with the experiment values due to the excessive idealization of DFT [67–69]. For all models, the bottom of CB is primarily derived from C 2p and N 2p and the top of VB was primarily constituted of N 2p. The cyano group and nitrogen vacancies result in a slight decrease of bandgap about eV for M1 and M2, which are essentially in accordance with the experimental. Notably, after introducing the P atom, an obvious impu-rity defect state emerged below CB of M4 was constituted of N p and P p orbitals. The introduction of defect states can change the transfer path of photogenerated electrons. Besides, the defect states could be an electron sink to accept the electrons that cannot reach the CB photoexcited from the VB. PKCN with the assistance of the defect state can utilize the photons with less energy than the bandgap, facilitating more light response Moreover, the defect states could accept the relaxation elec-trons from CB.
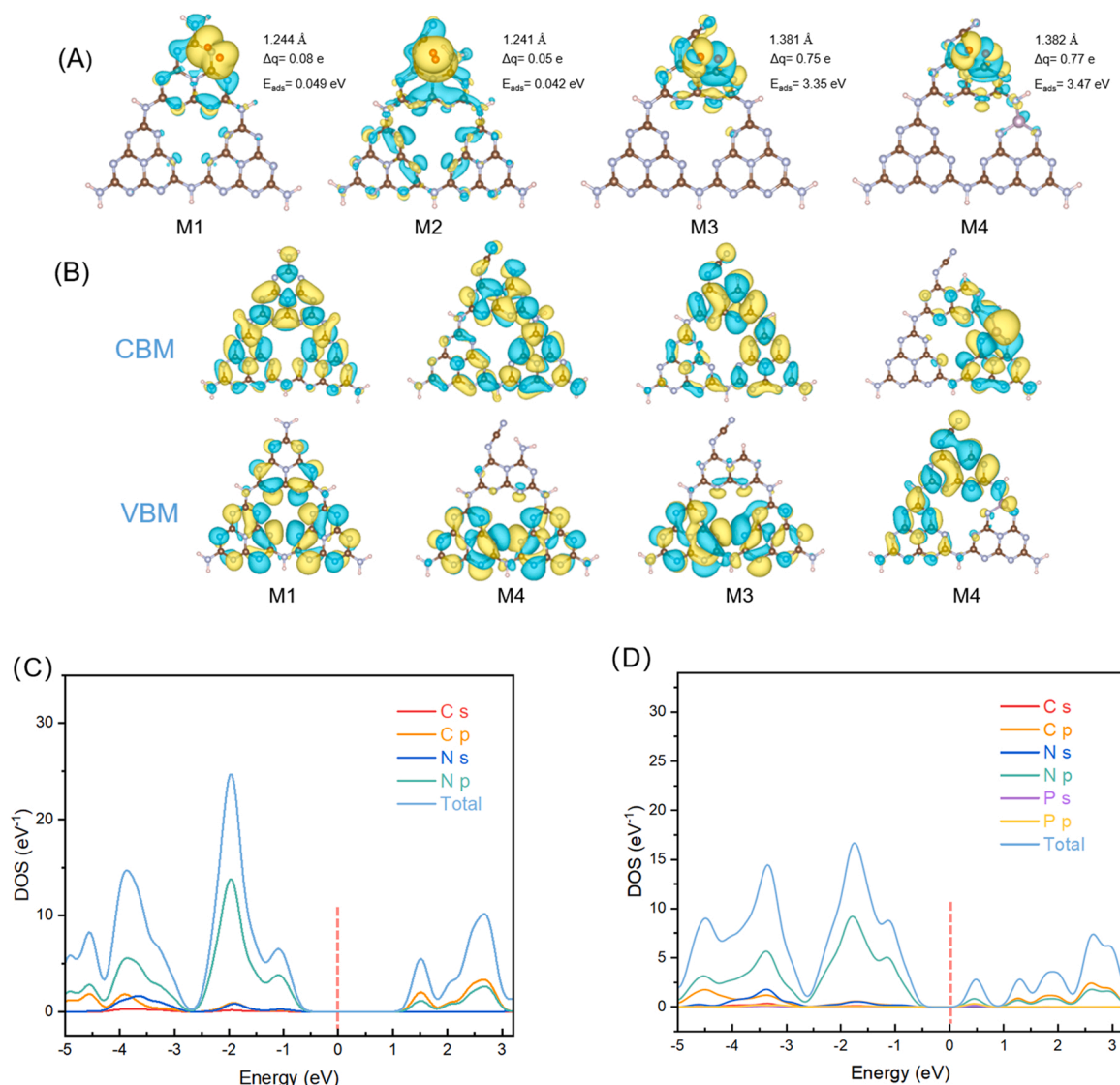
Fig. 9. (A) the top views of optimized oxygen adsorption. The blue part delegate the electron compact district and the yellow signifies the electron deficit. E_{ads} was the adsorption energy and Δq was total charge transfer for the oxygen; Isosurface values= 0.000133; (B) the electronic structure of M1, M2, M3, and M4 with corresponding charge distribution of VBM (valence band maximum) and CBM (conduction band minimum). The total density of states and partial density of states of M1 (C) and M4 (D), and the dashed red line is the Fermi level.

Based on the above analysis, we can draw the conclusion about the synergies of components: (1) The cyano group alters the charge distribution to create an internal electric field thus driving the migration of photoexcited carriers (2) Nitrogen vacancies significantly improve the adsorption capacity of catalyst to oxygen and provide the prerequisite for oxygen activation to generate reactive oxygen species. (3) K atoms shorten the distance between g-C$_3$N$_4$ layers and improve the conductivity, constructing an electron bridge to improve the charge flow between layers. (4) P atoms can insert an impurity defect state in the bandgap and change the transfer mode of photogenerated electrons.

Therefore, the singlet oxygen generation mechanism of PK10 is described in Fig. 10. Under the action of the electron bridge constructed by K atoms, the photoexcited charges could be fast transferred from VB to CB. Meanwhile, more photogenerated electrons can transfer and enter the reaction, enhancing the separation efficiency of photoexcited carriers. Three $^1O_2$ generation pathways can be summarized. In the pathway I, the abundant e$^-$ on CB reacts with O$_2$ that adsorbed by nitrogen vacancy to form $\bullet O_2^-$. Subsequently, $\bullet O_2^-$ further reacts with h$^+$ to form $^1O_2$. According to the above analysis, the pathway I plays a dominant role. In the pathway II, the P atom introduced an impurity

defect level below CB, which can accommodate electrons relaxed from CB. Besides, the photosensitivity of the catalyst was greatly enhanced and the energy barrier of $^1O_2$ generation was reduced. In the pathway III, the $\bullet O_2^-$ formed at CB was further converted to $^1O_2$ and H$_2$O$_2$. Besides, the pathway III plays a minimal role. Under the synergy of each active unit, PKCN owns excellent $^1O_2$ generation ability with three pathways.

3.7. Degradation pathways and toxicity analysis

The possible degradation pathways of ATZ in the PK10 system were investigated through the LC-MS and the mass curves of the substance at different reaction times were displayed (Fig. 11A and Fig. S17A-AC). It was obvious that the abundance of ATZ ($m/z = 216$) was invariant during the dark reaction process, while once the visible light was applied, its abundance significantly decreased and the abundance of intermediates changed continuously. Based on the previous studies and the m/z value, some possible major intermediates can be speculated (Table S6). In addition, according to the three probable pathways of ATZ degradation can be revealed based on the molecular structure of
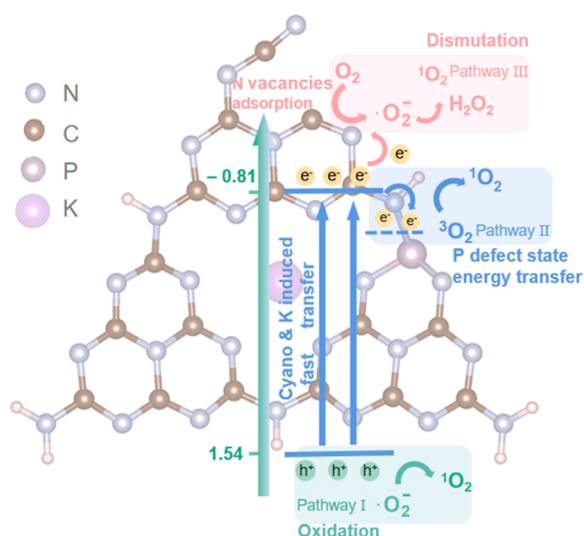
Fig. 10. schematic mechanisms of $^1O_2$ generation on PK10 for degradation of ATZ.

intermediates (Fig. 11A), and the variation curves of intermediate abundance in each pathway were plotted. In pathway I, the side chain of ATZ was rapidly attacked by ROS to form a -OH which was subsequently removed and transformed into A2 [70]. Subsequently, the branched chain was shortened and eventually converted to A5 with demethylation. In pathway II, the C-Cl bond of the ATZ molecule is easily, thereby it can be oxidized by ROS and then replaced and broken by −OH [71]. Then, an oxidation reaction and demethylation reaction similar to that in pathway I occur to obtain B4. In pathway III, the methyl group replaces the chlorine on the triazine ring firstly. Subsequently, serial demethylation and hydroxylation happened to obtain C3-C4. Finally, C5 was obtained by ring-opening reactions [72]. Considering the complexity of the transformation process of intermediates in the system, it is possible for the intermediates in each pathway to transform into each other. Therefore, C5 can be produced in other ways through the ring-opening reaction. Obviously, the abundance of pathway I was dominant, indicating this pathway was preferred in the reaction process.

To estimate the toxicity of the intermediates during the degradation, the acute toxicity and bioaccumulation factors of intermediates were predicted using the T.E.S.T. with a consistent approach and compared with ATZ. Fig. 11B exhibits the acute toxicity and bioaccumulation factor of intermediates by T.E.S.T (detailed information in Table S7) Obviously, ATZ owns the most hazardous to fathead minnow and
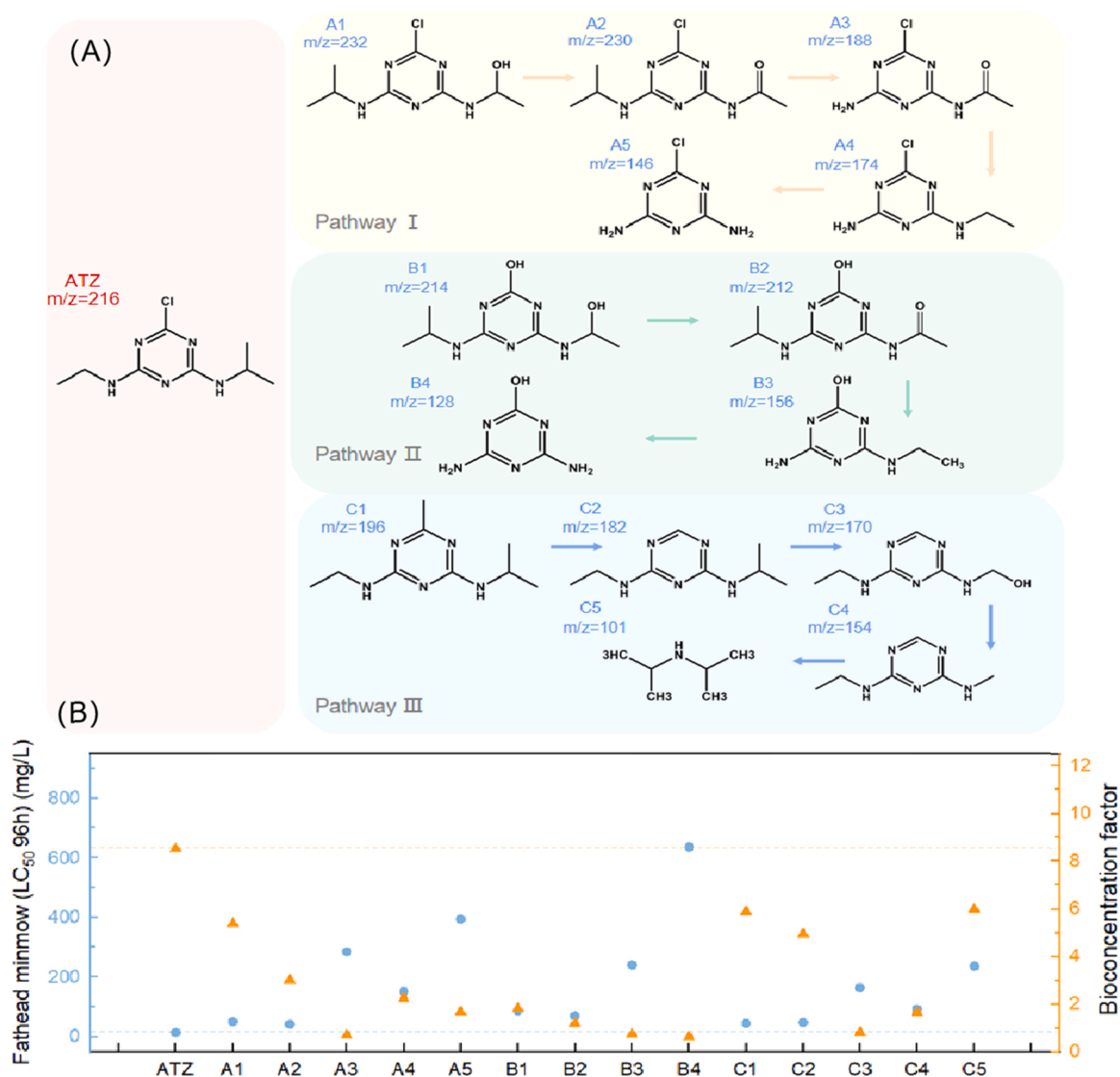

Fig. 11. (A) the possible three pathways of degradation; (B) the acute toxicity and bioconcentration factor of intermediates were estimated by T.E.S.T.

highest bioaccumulation factor. During the reaction process, the bioaccumulation factors of the main intermediates decreased significantly, suggesting that their ability to accumulate in organisms decreased [73]. To visualize and holistically represent intermediates toxicity, soybean culture experiments were carried out. Firstly, select healthy and strong soybean seeds after disinfection to germination. Then further select healthily and the same growth of soybean seedlings for culture in the nutrient solution (Fig. S18). After a few days of culture, soybean poisoning can begin at the double leaf stage (Fig. S19). Primary ATZ solution and degraded by PK10 for 15, 30, 45, 60, 90, and 120 min were used to configure a nutrient solution for subsequent culture. A week later, the growth status of soybean seedlings was analyzed and observed. As shown in Fig. S20, different degrees of damage can be found in the soybean seedlings, especially P15-P60 damage is the most serious, while P120 is almost no damage. Leaf chlorosis of P15 - P60 was observed ascribe to ATZ works mainly by inhibiting photosynthesis. In addition, the young leaves of P15 and P30 at the trefoil stage almost all died. The growth of P120 was almost unaffected, and the stem height and leaf size were both superior to P0, but the lignification of the stem was significantly weaker than P0. Moreover, the amount of chlorophyll was detected by the absorbance at 663 nm and 645 nm on UV–vis spectroscopy. And then the content of chlorophyll A and B can be calculated from the absorbance (detailed information in support information). Chlorophyll content at each stage as shown in Fig S21, and the degree of different damage to soybean was obvious. The chlorophyll content of the P120 sample was 2.53 mg/g, which was close to the normal value of soybean chlorophyll content (Fig. S22). This indicated that the toxicity of ATZ to soybean was within the safe range after degradation for 120 min. In conclusion, the PKCN can effectively remove ATZ by photocatalytic and greatly reduce the harm to the environment.

4. Conclusion

To sum up, P, K-doped g-C_3N_4 with cyano group and nitrogen vacancies was fabricated via a facile method to realize the efficient production of $^1O_2$. PKCN owns excellent photocatalytic degradation of ATZ, even up to 95% of ATZ degradation under optimized conditions (pH=5). Furthermore, three singlet oxygen generation paths of PKCN were demonstrated through experiments and analysis, namely hole oxidation, energy transfer and dismutation reaction. Among the three pathways, hole oxidation is the main reaction path. Besides, it has been determined that P atoms were the crucial component for singlet oxygen formation. Besides, the role of each active unit in photocatalysis was visualized by DFT calculation, and summarized the synergy: Cyano groups change the charge distribution and induce a built-in electric field; nitrogen vacancies significantly increase the oxygen adsorption capacity; K atoms increase the conductivity and build an electron bridge between layers; P atoms enhance the photosensitivity and introduce defect levels to decrease the energy transfer barrier. Furthermore, the ATZ degradation pathways and intermediates were investigated. The toxicity of the intermediate process was demonstrated by the T.E.S.T. and soybean culture experiment, and it was found that the toxicity was significantly reduced after 120 min degradation. The more detailed insight into the roles of each active unit and their synergistic effects would pave the way for rational custom preparation of g-C_3N_4.

CRediT authorship contribution statement

Yaocheng Deng: Conceptualization, Investigation, Writing – review & editing, Supervision and Funding acquisition. **Zhanpeng Zhou:** Methodology, Data curation, Original draft, Writing – original draft. **Hao Zeng:** VASP calculation, Revision. **Rongdi Tang:** Data analysis, Investigation. **Ling Li:** Investigation, Data analysis. **Jiajia Wang:** Investigation, Data analysis. **Chengyang Feng:** VASP calculation, Revision. **Daoxin Gong:** Formal analysis, Writing – review & editing. **Lin Tang:** Supervision, Writing – review & editing. **Ying Huang:**

Investigation, Supervision, Writing – review & editing. All authors contributed to the interpretation of the results and improvement of the paper.

Declaration of Competing Interest

The authors declare that they have no known competing financial interests or personal relationships that could have appeared to influence the work reported in this paper.

Data Availability

Data will be made available on request.

Appendix A. Supporting information

Supplementary data associated with this article can be found in the online version at doi:10.1016/j.apcatb.2022.121942.

References

[1] Y.H. Guan, J. Ma, Y.M. Ren, Y.L. Liu, J.Y. Xiao, L.Q. Lin, C. Zhang, Efficient degradation of atrazine by magnetic porous copper ferrite catalyzed peroxymonosulfate oxidation via the formation of hydroxyl and sulfate radicals, Water Res. 47 (2013) 5431–5438.

[2] H.J. Choi, D. Kim, T.J. Lee, Photochemical degradation of atrazine in UV and UV/ H_2O_2 process: pathways and toxic effects of products, J. Environ. Sci. Health B 48 (2013) 927–934.

[3] Z. Feng, Q. Tian, Q. Yang, Y. Zhou, H. Zhao, G. Zhao, Selectively photoelectrocatalytic reduction of oxygen to hydroxyl radical and singlet oxygen: mechanism and validation in coal wastewater, Appl. Catal. B 286 (2021), 119908.

[4] Y. Zheng, Z. Yu, F. Lin, F. Guo, K.A. Alamry, L.A. Taib, A.M. Asiri, X. Wang, Sulfur-doped carbon nitride polymers for photocatalytic degradation of organic pollutant and reduction of Cr(VI), Molecules 22 (2017).

[5] J. Brame, M. Long, Q. Li, P. Alvarez, Trading oxidation power for efficiency: differential inhibition of photo-generated hydroxyl radicals versus singlet oxygen, Water Res 60 (2014) 259–266.

[6] H. Kim, W. Kim, Y. Mackeyev, G.S. Lee, H.J. Kim, T. Tachikawa, S. Hong, S. Lee, J. Kim, L.J. Wilson, T. Majima, P.J. Alvarez, W. Choi, J. Lee, Selective oxidative degradation of organic pollutants by singlet oxygen-mediated photosensitization: tin porphyrin versus C60 aminofullerene systems, Environ. Sci. Technol. 46 (2012) 9606–9613.

[7] Y. Choi, Y. Ye, Y. Mackeyev, M. Cho, S. Lee, L.J. Wilson, J. Lee, P.J.J. Alvarez, W. Choi, J. Lee, C60 aminofullerene-magnetite nanocomposite designed for efficient visible light photocatalysis and magnetic recovery, Carbon 69 (2014) 92–100.

[8] X. Wang, K. Maeda, A. Thomas, K. Takanabe, G. Xin, J.M. Carlsson, K. Domen, M. Antonietti, A metal-free polymeric photocatalyst for hydrogen production from water under visible light, Nat. Mater. 8 (2009) 76–80.

[9] D. Liu, J. Wang, X. Bai, R. Zong, Y. Zhu, Self-assembled PDINH supramolecular system for photocatalysis under visible light, Adv. Mater. 28 (2016) 7284–7290.

[10] R. Tang, D. Gong, Y. Deng, S. Xiong, J. Deng, L. Li, Z. Zhou, J. Zheng, L. Su, L. Yang, π-π Stacked step-scheme PDI/g-C_3N_4/TiO_2@Ti_3C_2 photocatalyst with enhanced visible photocatalytic degradation towards atrazine via peroxymonosulfate activation, Chem. Eng. J. 427 (2022) 131809.

[11] R. Tang, D. Gong, Y. Deng, S. Xiong, J. Zheng, L. Li, Z. Zhou, L. Su, J. Zhao, pi-pi stacking derived from graphene-like biochar/g-C_3N_4 with tunable band structure for photocatalytic antibiotics degradation via peroxymonosulfate activation, J. Hazard. Mater. 423 (2022), 126944.

[12] Y. Deng, L. Tang, C. Feng, G. Zeng, Z. Chen, J. Wang, H. Feng, B. Peng, Y. Liu, Y. Zhou, Insight into the dual-channel charge-charrier transfer path for nonmetal plasmonic tungsten oxide based composites with boosted photocatalytic activity under full-spectrum light, Appl. Catal. B Environ. 235 (2018) 225–237.

[13] Y. Deng, C. Feng, L. Tang, Y. Zhou, Z. Chen, H. Feng, J. Wang, J. Yu, Y. Liu, Ultrathin low dimensional heterostructure composites with superior photocatalytic activity: Insight into the multichannel charge transfer mechanism, Chem. Eng. J. 393 (2020), 124718.

[14] G. Zhang, J. Zhang, M. Zhang, X. Wang, Polycondensation of thiourea into carbon nitride semiconductors as visible light photocatalysts, J. Mater. Chem. 22 (2012) 8083.

[15] H. Wang, X. Yang, W. Shao, S. Chen, J. Xie, X. Zhang, J. Wang, Y. Xie, Ultrathin black phosphorus nanosheets for efficient singlet oxygen generation, J. Am. Chem. Soc. 137 (2015) 11376–11382.

[16] H. Yu, R. Shi, Y. Zhao, T. Bian, Y. Zhao, C. Zhou, G.I.N. Waterhouse, L.Z. Wu, C. H. Tung, T. Zhang, Alkali-assisted synthesis of nitrogen deficient graphitic carbon nitride with tunable band structures for efficient visible-light-driven hydrogen evolution, Adv. Mater. 29 (2017), 1605148.

[17] Y. Li, S. Wang, W. Chang, L. Zhang, Z. Wu, S. Song, Y. Xing, Preparation and enhanced photocatalytic performance of sulfur doped terminal-methylated g-C3N4 nanosheets with extended visible-light response, J. Mater. Chem. A 7 (2019) 20640–20648.

[18] W. Li, Z. Wei, K. Zhu, W. Wei, J. Yang, J. Jing, D.L. Phillips, Y. Zhu, Nitrogen-defect induced trap states steering electron-hole migration in graphite carbon nitride, Appl. Catal. B 306 (2022), 121142.

[19] L. Chen, C. Chen, Z. Yang, S. Li, C. Chu, B. Chen, Simultaneously tuning band structure and oxygen reduction pathway toward high-efficient photocatalytic hydrogen peroxide production using cyano-rich graphitic carbon nitride, Adv. Funct. Mater. 31 (2021).

[20] S. Zhang, S. Song, P. Gu, R. Ma, D. Wei, G. Zhao, T. Wen, R. Jehan, B. Hu, X. Wang, Visible-light-driven activation of persulfate over cyano and hydroxyl group co-modified mesoporous g-C3N4 for boosting bisphenol A degradation, J. Mater. Chem. A 7 (2019) 5552–5560.

[21] M. Bellardita, E.I. García-López, G. Marcì, I. Krivtsov, J.R. García, L. Palmisano, Selective photocatalytic oxidation of aromatic alcohols in water by using P-doped g-C3N4, Appl. Catal. B 220 (2018) 222–233.

[22] W. Yan, L. Yan, C. Jing, Impact of doped metals on urea-derived g-C3N4 for photocatalytic degradation of anti38biotics: Structure, photoactivity and degradation mechanisms, Appl. Catal. B 244 (2019) 475–485.

[23] T. Xiong, W. Cen, Y. Zhang, F. Dong, Bridging the g-C3N4 interlayers for enhanced photocatalysis, ACS CataL. 6 (2016) 2462–2472.

[24] W. Li, Z. Guo, L. Jiang, L. Zhong, G. Li, J. Zhang, K. Fan, S. Gonzalez-Cortes, K. Jin, C. Xu, T. Xiao, P.P. Edwards, Facile in situ reductive synthesis of both nitrogen deficient and protonated g-C3N4 nanosheets for the synergistic enhancement of visible-light H2 evolution, Chem. Sci. 11 (2020) 2716–2728.

[25] Y. Kang, Y. Yang, L.C. Yin, X. Kang, G. Liu, H.M. Cheng, An amorphous carbon nitride photocatalyst with greatly extended visible-light-responsive range for photocatalytic hydrogen generation, Adv. Mater. 27 (2015) 4572–4577.

[26] L. Ge, C. Han, J. Liu, Novel visible light-induced g-C3N4/Bi2WO6 composite photocatalysts for efficient degradation of methyl orange, Appl. Catal. B 108 109 (2011) 100–107.

[27] Z. Xiong, Z. Wang, M. Muthu, Y. Zhang, Construction of an in-situ Fenton-like system based on a g-C3N4 composite photocatalyst, J. Hazard. Mater. 373 (2019) 565–571.

[28] S. Hu, L. Ma, J. You, F. Li, Z. Fan, F. Wang, D. Liu, J. Gui, A simple and efficient method to prepare a phosphorus modified g-C3N4 visible light photocatalyst, RSC Adv. 4 (2014) 21657–21663.

[29] Y. Zhang, M. Antonietti, Photocurrent generation by polymeric carbon nitride solids: an initial step towards a novel photovoltaic system, Chem. Asian J. 5 (2010) 1307–1311.

[30] Z. Wei, M. Liu, Z. Zhang, W. Yao, H. Tan, Y. Zhu, Efficient visible-light-driven selective oxygen reduction to hydrogen peroxide by oxygen-enriched graphitic carbon nitride polymers, Energy Environ. Sci. 11 (2018) 2581–2589.

[31] V.W. Lau, I. Moudrakovski, T. Botari, S. Weinberger, M.B. Mesch, V. Duppel, J. Senker, V. Blum, B.V. Lotsch, Rational design of carbon nitride photocatalysts by identification of cyanamide defects as catalytically relevant sites, Nat. Commun. 7 (2016) 12165.

[32] X. Ma, Y. Lv, J. Xu, Y. Liu, R. Zhang, Y. Zhu, A strategy of enhancing the photoactivity of g-C3N4 via doping of nonmetal elements: a first-principles, Study, J. Phys. Chem. C 116 (2012) 23485–23493.

[33] T. Sano, S. Tsutsui, K. Koike, T. Hirakawa, Y. Teramoto, N. Negishi, K. Takeuchi, Activation of graphitic carbon nitride (g-C3N4) by alkaline hydrothermal treatment for photocatalytic NO oxidation in gas phase, J. Mater. Chem. A 1 (2013) 6489.

[34] H. Gao, S. Yan, J. Wang, Y.A. Huang, P. Wang, Z. Li, Z. Zou, Towards efficient solar hydrogen production by intercalated carbon nitride photocatalyst, Phys. Chem. Chem. Phys. 15 (2013) 18077–18084.

[35] G. Xu, Y. Liang, F. Chen, Continuously photocatalytic production of H2O2 with high concentrations using 2-ethylanthraquinone as photocatalyst, J. Mol. Catal. A Chem. 420 (2016) 66–72.

[36] G. Zhang, M. Zhang, X. Ye, X. Qiu, S. Lin, X. Wang, Iodine modified carbon nitride semiconductors as visible light photocatalysts for hydrogen evolution, Adv. Mater. 26 (2014) 805–809.

[37] Y. Li, M. Gu, M. Zhang, X. Zhang, K. Lv, Y. Liu, W. Ho, F. Dong, C3N4 with engineered three coordinated (N3C) nitrogen vacancy boosts the production of 1O2 for Efficient and stable NO photo-oxidation, Chem. Eng. J. 389 (2020), 124421.

[38] K. Chu, Y. Luo, P. Shen, X. Li, Q. Li, Y. Guo, Unveiling the synergy of O-vacancy and heterostructure over MoO3−x/MXene for N2 electroreduction to NH3, Adv. Energy Mater. 12 (2021).

[39] K.L. Corp, C.W. Schlenker, Ultrafast spectroscopy reveals electron-transfer cascade that improves hydrogen evolution with carbon nitride photocatalysts, J. Am. Chem. Soc. 139 (2017) 7904–7912.

[40] S. Wu, H. Yu, S. Chen, X. Quan, Enhanced photocatalytic H2O2 production over carbon nitride by doping and defect engineering, ACS Catal. 10 (2020) 14380–14389.

[41] L. Shi, L. Yang, W. Zhou, Y. Liu, L. Yin, X. Hai, H. Song, J. Ye, Photoassisted construction of holey defective g-C3N4 photocatalysts for efficient visible-light-driven H2O2 production, Small 14 (2018), 1703142.

[42] Z. Zhang, Y. Huang, K. Liu, L. Guo, Q. Yuan, B. Dong, Multichannel-improved charge-carrier dynamics in well-designed hetero-nanostructural plasmonic photocatalysts toward highly efficient solar-to-fuels conversion, Adv. Mater. 27 (2015) 5906–5914.

[43] J. Yuan, X. Liu, Y. Tang, Y. Zeng, L. Wang, S. Zhang, T. Cai, Y. Liu, S. Luo, Y. Pei, C. Liu, Positioning cyanamide defects in g-C3N4: Engineering energy levels and active sites for superior photocatalytic hydrogen evolution, Appl. Catal. B 237 (2018) 24–31.

[44] S. Wang, B.Y. Guan, X.W.D. Lou, Construction of ZnIn2S4-In2O3 hierarchical tubular heterostructures for efficient CO2 photoreduction, J. Am. Chem. Soc. 140 (2018) 5037–5040.

[45] Y. Deng, L. Tang, G. Zeng, Z. Zhu, M. Yan, Y. Zhou, J. Wang, Y. Liu, J. Wang, Insight into highly efficient simultaneous photocatalytic removal of Cr(VI) and 2,4-diclorophenol under visible light irradiation by phosphorus doped porous ultrathin g-C3N4 nanosheets from aqueous media: Performance and reaction mechanism, Appl. Catal. B 203 (2017) 343–354.

[46] D. Li, C. Wen, J. Huang, J. Zhong, P. Chen, H. Liu, Z. Wang, Y. Liu, W. Lv, G. Liu, High-efficiency ultrathin porous phosphorus-doped graphitic carbon nitride nanosheet photocatalyst for energy production and environmental remediation, Appl. Catal. B 307 (2022), 121099.

[47] B.Y. Yang, Y. Cao, F.F. Qi, X.Q. Li, Q. Xu, Atrazine adsorption removal with nylon6/polypyrrole core-shell nanofibers mat: possible mechanism and characteristics, Nanoscale Res. Lett. 10 (2015) 207.

[48] G. Li Puma, A. Brucato, Dimensionless analysis of slurry photocatalytic reactors using two-flux and six-flux radiation absorption–scattering models, Catal. Today 122 (2007) 78–90.

[49] G. Li Puma, Dimensionless analysis of photocatalytic reactors using suspended solid photocatalysts, Chem. Eng. Res. Des. 83 (2005) 820–826.

[50] D. Dolat, N. Quici, E. Kusiak-Nejman, A.W. Morawski, G. Li Puma, One-step, hydrothermal synthesis of nitrogen, carbon co-doped titanium dioxide (N,CTiO2) photocatalysts. Effect of alcohol degree and chain length as carbon dopant precursors on photocatalytic activity and catalyst deactivation, Appl. Catal. B 115–116 (2012) 81–189.

[51] Y. Zhou, J. Jiang, Y. Gao, J. Ma, S.Y. Pang, J. Li, X.T. Lu, L.P. Yuan, Activation of peroxymonosulfate by benzoquinone: a novel nonradical oxidation process, Environ. Sci. Technol. 49 (2015) 12941–12950.

[52] H. Shao, X. Zhao, Y. Wang, R. Mao, Y. Wang, M. Qiao, S. Zhao, Y. Zhu, Synergetic activation of peroxymonosulfate by Co3O4 modified g-C3N4 for enhanced degradation of diclofenac sodium under visible light irradiation, Appl. Catal. B 218 (2017) 810–818.

[53] I. Papailias, N. Todorova, T. Giannakopoulou, N. Ioannidis, P. Dallas, D. Dimotikali, C. Trapalis, Novel torus shaped g-C3N4 photocatalysts, Appl. Catal. B 268 (2020), 118733.

[54] L. Xu, L. Li, L. Yu, J.C. Yu, Efficient generation of singlet oxygen on modified g-C3N4 photocatalyst for preferential oxidation of targeted organic pollutants, Chem. Eng. J. 431 (2022), 134241.

[55] R. Tang, D. Gong, Y. Zhou, Y. Deng, C. Feng, S. Xiong, Y. Huang, G. Peng, L. Li, Z. Zhou, Unique g-C3N4/PDI-g-C3N4 homojunction with synergistic piezo-photocatalytic effect for aquatic contaminant control and H2O2 generation under visible light, Appl. Catal. B 303 (2022), 120929.

[56] H. Kim, C.E. Choong, I. Han, C.M. Park, I.W. Nah, J.R. Kim, B.H. Jeon, Y. Yoon, M. Jang, Insight into the role of charge carrier mediation zone for singlet oxygen production over rod-shape graphitic carbon nitride: Batch and continuous-flow reactor, J. Hazard. Mater. 424 (2022), 127652.

[57] Y. Nosaka, A.Y. Nosaka, Generation and detection of reactive oxygen species in photocatalysis, Chem. Rev. 117 (2017) 11302–11336.

[58] D. Zhang, P. Wang, J. Wang, Y. Li, Y. Xia, S. Zhan, Tailoring of electronic and surface structures boosts exciton-triggering photocatalysis for singlet oxygen generation, Proc. Natl. Acad. Sci. USA 118 (2021).

[59] H. Wang, S. Jiang, S. Chen, D. Li, X. Zhang, W. Shao, X. Sun, J. Xie, Z. Zhao, Q. Zhang, Y. Tian, Y. Xie, Enhanced singlet oxygen generation in oxidized graphitic carbon nitride for organic synthesis, Adv. Mater. 28 (2016) 6940–6945.

[60] D. Li, X. Li, T. Zhao, H. Liu, S. Jiang, Q. Zhang, H. Agren, G. Chen, Ultraefficient singlet oxygen generation from manganese-doped cesium lead chloride perovskite quantum dots, ACS Nano 14 (2020) 12596–12604.

[61] C. Schweitzer, R. Schmidt, Physical mechanisms of generation and deactivation of singlet oxygen, Chem. Rev. 103 (2003) 1685–1757.

[62] Q. Zheng, E. Xu, E. Park, H. Chen, D. Shuai, Looking at the overlooked hole oxidation: photocatalytic transformation of organic contaminants on graphitic carbon nitride under visible light irradiation, Appl. Catal. B 240 (2019) 262–269.

[63] D. Lei, J. Xue, X. Peng, S. Li, Q. Bi, C. Tang, L. Zhang, Oxalate enhanced synergistic removal of chromium(VI) and arsenic(III) over ZnFe2O4/g-C3N4: Z-scheme charge transfer pathway and photo-Fenton like reaction, Appl. Catal. B 282 (2021), 1195778.

[64] G.-h Moon, M. Fujitsuka, S. Kim, T. Majima, X. Wang, W. Choi, Eco-friendly photochemical production of H2O2 through O2 reduction over carbon nitride frameworks incorporated with multiple heteroelements, ACS Catal. 7 (2017) 2886–2895.

[65] Y. Li, Y. Fang, Z. Cao, N. Li, D. Chen, Q. Xu, J. Lu, Construction of g-C3N4/PDI@ MOF heterojunctions for the highly efficient visible light-driven degradation of pharmaceutical and phenolic micropollutants, Appl. Catal. B 250 (2019) 150–162.

[66] J. Li, L. Cai, J. Shang, Y. Yu, L. Zhang, Giant enhancement of internal electric field boosting bulk charge separation for photocatalysis, Adv. Mater. 28 (2016) 4059–4064.

[67] F. Wei, Y. Liu, H. Zhao, X. Ren, J. Liu, T. Hasan, L. Chen, Y. Li, B.L. Su, Oxygen self-doped g-C$_3$N$_4$ with tunable electronic band structure for unprecedentedly enhanced photocatalytic performance, Nanoscale 10 (2018) 4515–4522.

[68] Z.-F. Huang, J. Song, L. Pan, Z. Wang, X. Zhang, J.-J. Zou, W. Mi, X. Zhang, L. Wang, Carbon nitride with simultaneous porous network and O-doping for efficient solar-energy-driven hydrogen evolution, Nano Energy 12 (2015) 646–656.

[69] C. Feng, L. Tang, Y. Deng, J. Wang, Y. Liu, X. Ouyang, H. Yang, J. Yu, J. Wang, A novel sulfur-assisted annealing method of g-C$_3$N$_4$ nanosheet compensates for the loss of light absorption with further promoted charge transfer for photocatalytic production of H$_2$ and H$_2$O$_2$, Appl. Catal. B 281 (2021) 119539.

[70] G. Ye, P. Luo, Y. Zhao, G. Qiu, Y. Hu, S. Preis, C. Wei, Three-dimensional Co/Ni bimetallic organic frameworks for high-efficient catalytic ozonation of atrazine: Mechanism, effect parameters, and degradation pathways analysis, Chemosphere 253 (2020), 126767.

[71] C. Li, Y. Huang, X. Dong, Z. Sun, X. Duan, B. Ren, S. Zheng, D.D. Dionysiou, Highly efficient activation of peroxymonosulfate by natural negatively-charged kaolinite with abundant hydroxyl groups for the degradation of atrazine, Appl. Catal. B 247 (2019) 10–23.

[72] Z. Shen, H. Zhou, Z. Pan, Y. Guo, Y. Yuan, G. Yao, B. Lai, Degradation of atrazine by Bi$_2$MoO$_6$ activated peroxymonosulfate under visible light irradiation, J. Hazard. Mater. 400 (2020), 123187.

[73] J. Pan, B. Gao, P. Duan, K. Guo, X. Xu, Q. Yue, Recycling exhausted magnetic biochar with adsorbed Cu^{2+} as a cost-effective permonosulfate activator for norfloxacin degradation: Cu contribution and mechanism, J. Hazard. Mater. 413 (2021), 125413.